國 立 交 通 大 學

電信工程研究所

碩 士 論 文

用以激發電路板輻射地緣電流之

新微波元件:輻射電流驅動器

A New Microwave Component (*Current Driver*)
for Inducing Radiating Ground Edge Current in a
Printed Circuit Board

研究生：劉財溢 (Tsai-I Liu)

指導教授：鍾世忠 教授 (Dr. Shyh-Jong Chung)

中 華 民 國 九 十 九 年 七 月

用以激發電路板輻射地緣電流之新微波元件:輻射電流驅動器

A New Microwave Component (*Current Driver*) for Inducing Radiating Ground Edge Current in a Printed Circuit Board

研究生：劉財溢　　Student : Tsai-I Liu

指導教授：鍾世忠 博士　　Advisor : Dr. Shyh-Jong Chung

國立交通大學

電信工程研究所

碩士論文

A Thesis

Submitted to Institute of Communication Engineering

College of Electrical and Computer Engineering

National Chiao Tung University

in Partial Fulfillment of the Requirements

For the Degree of Master of Science

In Communication Engineering

July 2009

Hsinchu, Taiwan, Republic of China

中華民國 九十九年七月

用以激發電路板輻射地緣電流之新微波元件:輻射電流驅動器

研究生：劉財溢　　指導教授：鍾世忠 博士

電信工程研究所

碩士論文

摘要

在本論文中，我們提出一種名為電流驅動器之新型微波元件來激發地緣輻射電流。由於電流驅動器本身只作為一種小型的饋入裝置來將能量有效地饋入接地面產生輻射，因此對整體輻射的貢獻量很小，所以驅動器的尺寸可以設計得十分小而不影響整體天線特性。此種激發地緣電流作為輻射源的作法，相對於一般縮小化天線設計來說，在大幅地減小天線設計空間的同時，也不影響整體的輻射特性。此外本論文引用一種縮小化的巴倫等效電路模型來解釋電流驅動器的地緣電流產生機制並用來設計電流驅動器。在論文中，我們亦針對常用於隔離電磁干擾的金屬屏蔽盒對電流驅動器的特性影響做探討。結果指出即使在屏蔽盒緊臨電流驅動器的情況下，對驅動器的整體特性影響也不大。這顯示出電流驅動器在小型無線裝置的設計彈性。

基於上述的電流驅動器的優點，本論文提出二種基於電流驅動器的天線應用，此二種架構皆製作在常用的 FR4 基板上。首先我們設計應用於 WLAN 2.4 GHz 的電流驅動器，此驅動器可利用集總電容或者是指插式電容來實現，整體尺寸僅 4 mm × 4 mm，並具備良好的天線輻射特性。在 2.45 GHz 時，量測的天線輻射效率大於 60 %，並且在其接近全向性的平面上，量測的平均增益接近 0 dBi。接下來，我們藉由合併二個單頻的電流驅動器來達成雙頻 WLAN 2.4/5.2 GHz 操作，整體

尺寸為 8.5 mm × 4 mm。我們將在論文中詳細呈現雙頻電流驅動器的設計流程。量測的天線特性在低頻 2.45 GHz 時與先前提出的單一 2.4 GHz 的電流驅動器特性大致相符，具有接近全向性的場型與大於 60%的天線輻射效率。而在高頻 5.2 GHz 時，由於 FR4 基板在高頻的介質損耗，量測的天線效率降低至 50%左右，但仍然保持接近全向性的場型。實際量測結果與模擬結果相當吻合。由於利用電流驅動器來達成天線應用具有小尺寸且具備良好的天線輻射特性等優點，因此很適合應用於無線通訊系統。

A New Microwave Component (*Current Driver*) for Inducing Radiating Ground Edge Current in a Printed Circuit Board

Student : Tsai-I Liu Advisor : Dr. Shyh-Jong Chung

Institute of Communication Engineering
National Chiao Tung University

ABSTRACT

In this thesis, a new microwave component named current driver is proposed, which is capable of inducing ground edge current for radiation. Since the current driver serves as a small feeding structure with little contribution to radiation, it can be designed very small while good radiation properties are maintained. Compared to the miniaturized antennas, the approach that utilizes ground plane as the main radiation has smaller size and better antenna performance. Furthermore, a circuit model of the miniaturized balun (balanced to unbalanced transformer) is introduced to explain the current inducing mechanism and to provide some valuable physical insights into the properties of the current driver. The effect of a shielding metal box for the proximity circuitry near the current driver is also investigated. It is shown that the nearby shielding box has minor effect on the performance of the driver, which demonstrates the feasibility of the current driver for antenna applications in a compact wireless terminal.

Given the benefits shown above, two antenna applications based on the current driver are presented. Both of them are fabricated on the low cost FR4 substrate of 0.4 mm. First, the current driver for WLAN 2.4 GHz designed with a lumped capacitor or printed capacitor has a small size of about 4 mm × 4 mm. The good radiation properties are obtained at 2.45 GHz with the measured radiation efficiency over 60 % and the nearly omni-directional radiation pattern with the average gain of about 0 dBi. Secondly, the dual-band current driver for WLAN 2.4/5/2 GHz applications is achieved by combining two single-band current drivers with the overall size of about 8.5 mm × 4 mm. The measured radiation performances at 2.4 GHz are similar to the ones for the previous

single 2.4 GHz current driver, which has the measured antenna radiation efficiency higher than 60 % and nearly omin-directional patterns. At 5.2 GHz, the measured radiation efficiency is reduced to about 50 % due to the high dielectric loss caused by the FR4 substrate in the high frequency. The nearly omni-directional patterns are still maintained. The simulation and measurement results come to a great agreement. Based on the compactness and design flexibilities, the current driver is feasible for wireless applications

Acknowledgement

從專題生開始到碩士論文完成的這三年多，需要感謝的人很多。首先要感謝的就是指導老師鍾世忠教授，從專題的去耦合電路開始到碩士論文的電流驅動器研究，老師在各方面都給予許多詳盡的指導，幫助我理清許多天線觀念以及培養做研究的態度及方法。另外要感謝的就是已畢業的阿信學長、菁偉學姊、還有博士班的靖凱和肇堂學長以及研究助理柯柯，他們對我的碩士論文的啟發與發展幫助許多，可以說沒有他們我的碩士論文也無法這麼順利的完成。另外需要感謝的人還有實驗室助理珮華，許多麻煩的事都幸虧有她的幫忙聯絡及處理才能順利解決。

當然，也感謝一起畢業的碩二同學：逼逼、冷肥、楊子嫻、Toresa、Arno和阿凱，以及學弟妹：志謙、Kimi、老甘、瑋哥、阿澤、以及人豪，另外還有已畢業的少華、浩宇、小池、柏翔和阿彬，沒有他們，想必這三年在LAB 912的生活將會失色不少。

CONTENTS

CONTENTS OF TABLES

CONTENTS OF FIGURES

Chapter 1 INTRODUCTION

1-1 Background and Motivation

TABLE I

THE IEEE STANDARDS OF 802.11 A/B/G/N

802.11 Protocol	Release	Freq. (GHz)	Typ. Throughput (Mbit/s)	Max net bitrate (Mbit/s)	Mod.	MIMO	$r_{in.}$ (m)	$r_{out.}$ (m)
–	1997	2.4	0.9	2	DSSS, FHSS	×	~20	~100
a	1999	5	23	54	OFDM	×	~35	~120
b	1999	2.4	4.3	11	DSSS	×	~38	~140
g	2003	2.4	19	54	OFDM, DSSS	×	~38	~140
n	2009	2.4/5	74	248	OFDM	○	~70	~250

With the rapid development of personal computers (PCs), the demand for wireless communication between different terminals has seen growing importance. Since 1997, IEEE 802.11 group has been established several standards for WLAN (Wireless Local Area Network) applications. Detailed information for these standards is listed in TABLE I. As seen in the table, the data rate and transmission distance are greatly improved with the lanuch of new protocal. To achieve good communication quality, the antenna radiation property is also very important. However, there is a very limited space reserved for the antenna design due to the demand of compact devices in many wireless applications. Thus, antenna miniaturization is necessary to integrate the antenna in the restricted small circuit board area. However, it is challenging to scale down the antenna size while maintaining good antenna properties.

1-2 Literature Survey

To meet the market demands of device compactness, the subject of antenna miniaturization has been extensively investigated in various literatures. As has been shown in [1-3], some techniques applied to the substrate were utilized for antenna size reduction including the magneto-dielectric composite substrate and the embedded-circuit metasubstrate. However, the cost of the fabrication of these substrates is quite high, so they are not practical for real commercial applications. Electrically small antennas (ESAs), for example small dipole and loop antennas, are easily to be integrated into the circuit, but the external matching circuit is required because of the highly reactive impedance of the ESAs. Although the aforementioned drawbacks can be circumvented by placing a parasitic element near the ESAs to achieve resonance and impedance matching simultaneously in a small area to approach the theoretically lower bound of the quality factor Q [4-5], the bandwidth is still limited by the overall size. Planar inverted-F antennas (PIFAs) are popular because they provide the great degree of design flexibility to achieve multiband and compactness. The PIFA antenna with a spiraling tail or a capacitive loading is capable of dual-band operation with about 50% size of the conventional one [6]. In [7-10], the compact resonant antennas are designed by employing the composite Right/Left-handed transmission line.

The above-mentioned antenna miniaturization techniques mostly focus on the geometry modification. However, antenna size has fundamental limitations with consideration about gain, bandwidth, and efficiency [11-13]. To achieve better antenna properties, the finite ground plane on the PCB (printed circuit board) has to be considered in the antenna design process. In [14], the performance of the mobile phone for GSM 900/1800 operation was analyzed by the combination of two coupled resonators, the antenna and the chassis (finite length ground plane). The results indicated that the chassis is dominant in contribution of radiation in the lower frequency band. With the increasing knowing of the finite ground plane as a radiator, there are various techniques applied to the ground plane for better antenna performance, such as cutting slots [14-15], using wave traps [16], and adding ground edge current choke (GECC) [17]. In Fig. 1.1, the slots cut on the ground edge is used to extend the current path along the ground edge, which can effectively reduce the resonance frequency of the ground plane for better

antenna property in the lower band. Fig. 1.2 shows that the wavetraps are used to electrically reduce the ground size by blocking the ground edge current. The wavetrap is formed by a short circuited quarter-wavelength transmission line. When the wavetraps is in resonance, the impedance looking into the wavetrap is a open circuit. Therefore, the wavetraps can stop the edge current from flowing further and increase the resonance frequency of the ground plane. This is helpful to improve the antenna performance in the higher band. The current choke composed of the printed inductor and capacitor can perform a similar function as wavetraps but with a more compact size. Fig. 1.3 shows the monopole antenna with two chokes on the ground edge. The radiation patterns are improved by limiting the ground edge current with current chokes.

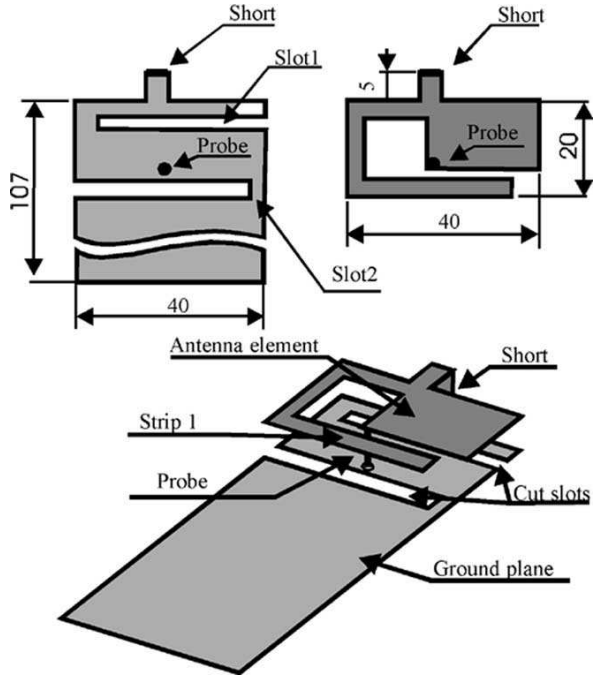

Fig. 1.1. Configuration for a PIFA with cutting slots on the ground edge.

To date, we have known that the ground plane can be used in the antenna design, but the challenge is how to effectively utilize the ground plane for main radiation. Some attempts that utilize the ground plane as the main radiator were published. Coupler-element based antenna designs can excite the chassis resonant mode so that the whole ground plane can radiate effectively [18-19]. Fig. 1.4 shows the configurations of the coupler-based antenna design. To excite the half wavelength resonance mode of the

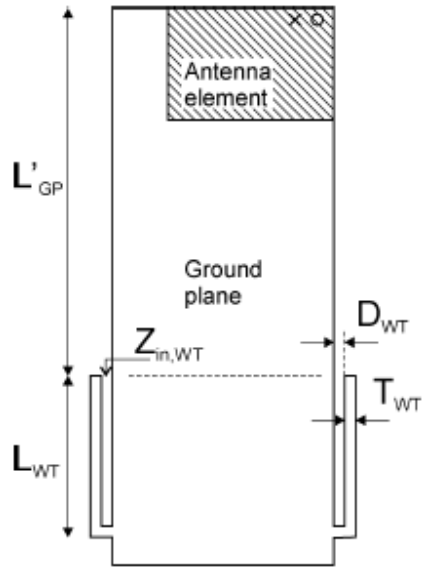

Fig. 1.2. Configuration for a PIFA antenna with wavetraps on the ground edge.

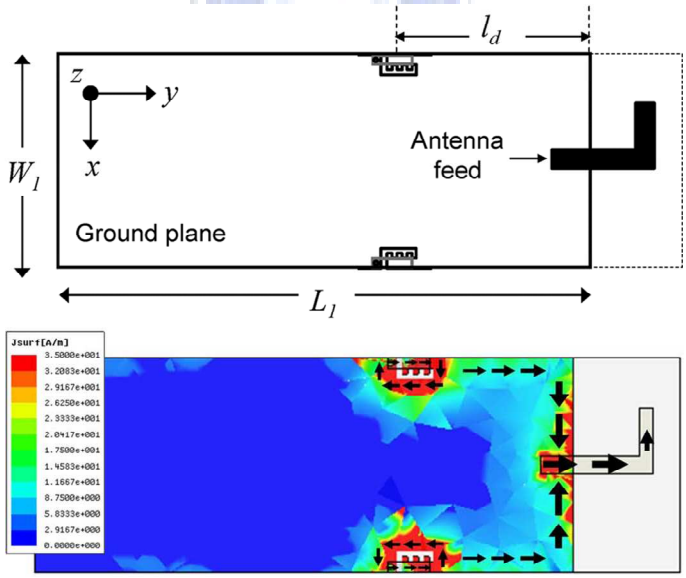

Fig. 1.3. Configuration and simulated current distribution for a monopole antenna with current chokes on the ground edge.

ground plane, the coupler is placed on the ground edge to couple to the ground plane by capacitive coupling. Nevertheless, the position, size and shape of the coupler are restricted for appropriate capacitive coupling. As seen in the figure, the coupler designed in Model 1 is bended to have better performance than the coupler designed in Model 2. However, this will increase the cost due to the fabrication difficulties. Also, these coupler

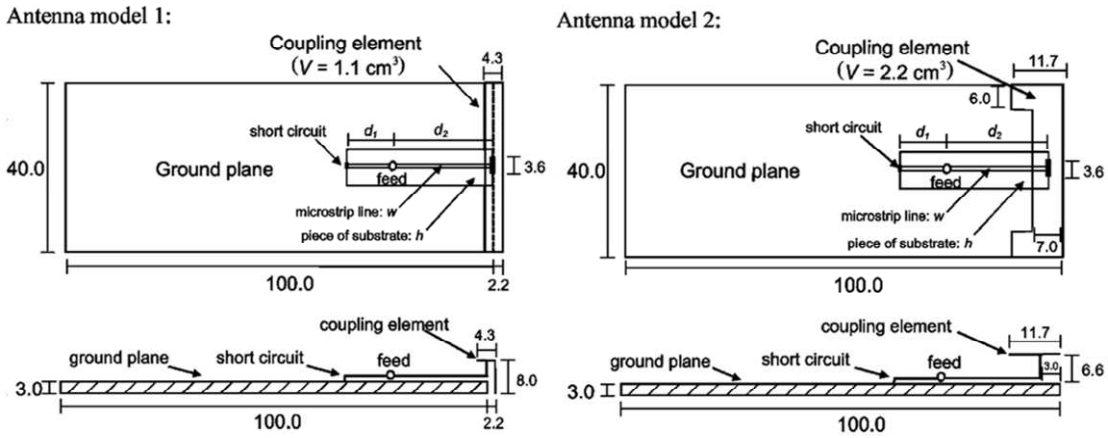

Fig. 1.4. Configuration of two coupler-based antennas

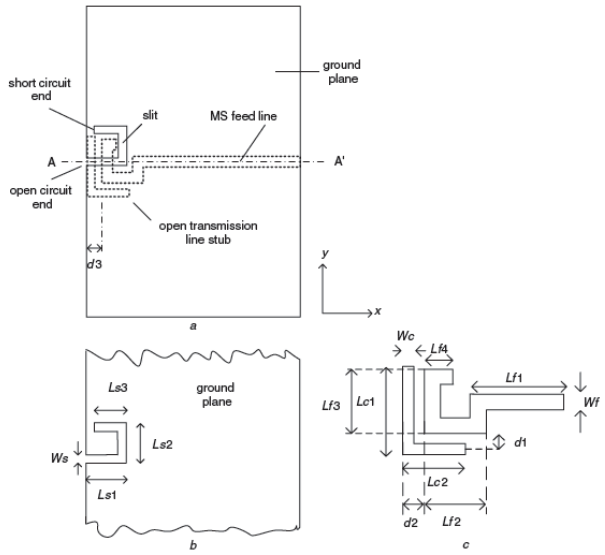

Fig. 1.5. Configuration of a miniaturized slot antenna loaded with bended open end transmission line stub.

based antennas are still bulky due to the need of additional matching circuit. Traditional microstrip-fed quarter-wavelength slot antennas cut on the ground edge, or their miniaturized versions, are easy to induce radiating edge current. Since the current is highly concentrated along the slot, some current leaking into the ground edge will also contribute partial radiation. Figure 1.5 shows the configuration of a miniaturized slot antenna loaded with bended open end transmission line stub. The capacitive loading is used to cancel the inductive reactance introduced by the reduced slot antenna so that the impedance can be well matched. It must be noticed that the radiation contribution from

the slot antenna is lowered with the slot size reduction but the portion of the radiation 5caused by the ground plane increases. However, these slot antennas are still responsible for partial radiation so the size reduction is limited even with the capacitive loading or external matching circuit employed [20-23].

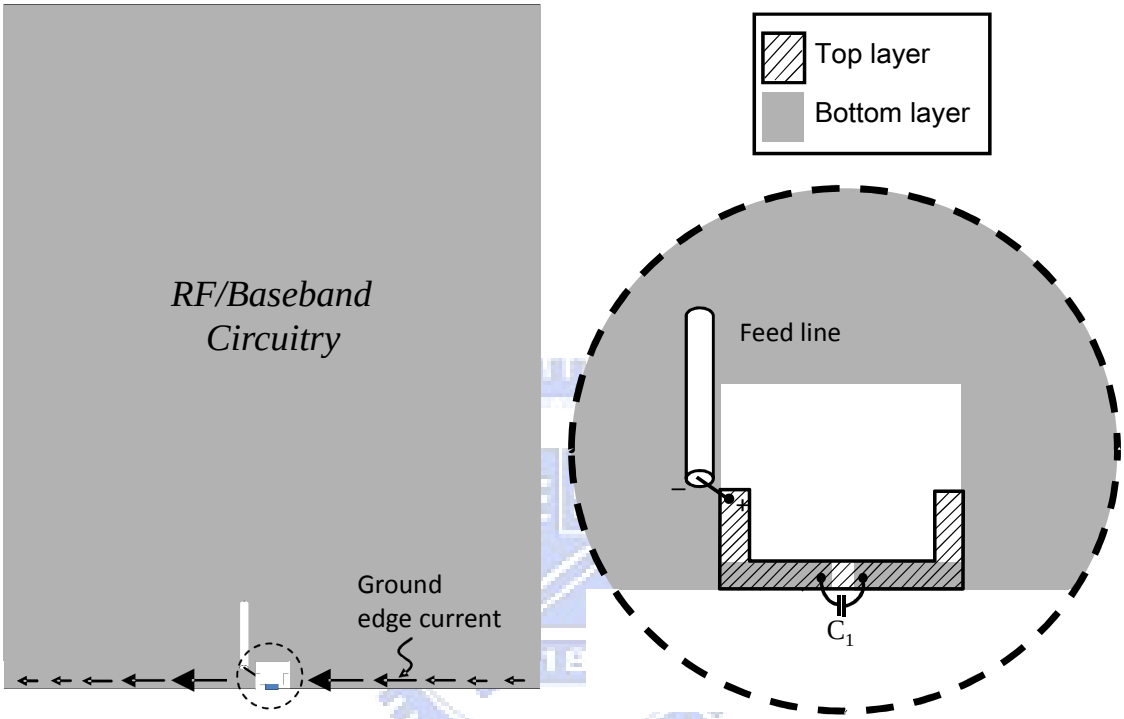

Fig. 1.6. Configuration of the current driver.

1-3 Contribution

In this thesis, a new microwave component as shown in Fig. 1.6, named *current driver*, is proposed to activate the ground current flowing along the circuit board edge for radiation. Since the current driver mainly works to transform the input RF signal into the ground edge current and has little responsibility for radiation, the current driver can be designed as small as possible without the necessity to consider much about the degradation of antenna radiation performance. The central idea underlying the design of the current driver is to divide the ground plane into two parts so that the RF signal can be fed in between the parts, without being short circuited, to excite the radiating edge currents. This idea was actually realized in the previous investigations. As shown in [23],

the ground plane is physically separated so that the ground plane can be fed as a thick dipole antenna with the external feeding network to achieve impedance matching. However, physically separation of the ground plane is impractical for many applications. In the present study, the ground plane is electrically separated by the proposed compact current driver, which is composed of a very small slot at the edge, a short coupling strip, and a lumped capacitor connected in between the slot. Without the need of the additional matching circuit, the current driver can be matched by appropriately coupling the RF signal to the ground edge through broadside coupling. The equivalent circuit model for the current driver is regarded as a miniaturized planar balun with the differential ports connected to the ground edge [24]. Thus, the ground edge current behaves similar to a dipole antenna fed by the miniaturized balun. Compared with the previously works, the size of the current driver is very small, which is only 3% × 3% of the space wavelength. Moreover, two current drivers can be combined together for dual-band operation. Through the simple design procedures, two resonances with good impedance matching are obtained.

1-4 Thesis organization

This thesis is organized as follows. Chapter II provides the theory of the planar miniaturized marchand balun. In Chapter III, the current driver for single band operation is proposed. The corresponding equivalent circuit model is derived by geometry observation, and the current driver is designed by structure parameter and ground size study. Moreover, the effect of the metal shielding box near the current driver is considered. Another configuration for the current driver with a printed capacitor is also developed. At the end of this chapter, the experiment results and the related discussion are presented. In Chapter IV, the dual-band operation for the current driver is achieved by combining two sing-band current drivers. Thoughtful design procedure for the design of the dual-band current driver is presented. The experiment results are also presented in this chapter. Finally, Section V gives the conclusions.

Chapter 2 THEORY OF MARCHAN BALUN

Baluns (balance to unbalance transformer), which can convert the unbalanced signal into the balanced one and also provide impedance transformation, are key components in many applications, such as double balanced mixers, push pull amplifiers, and feeding circuits for balanced antennas. Among them, Marchand balun is the most commonly used balun in microwave circuit, which can be implemented by transmission lines [25] or coupled lines [26-27]. This chapter focuses on the theory of the planar Marchand balun and its miniaturized version with lumped capacitor. Through the analysis of even- and odd-mode half circuit, it shows that the size of Marchand balun can be effectively reduced with the help of a lumped capacitor.

Fig. 2.1 shows the structure of conventional planar Marchand balun, which comprises of two sections of λ/4 coupled lines at the center frequency. However, the size of the conventional Marchand balun makes it impractical for lower band applications. In [24], the balun employs a lumped capacitor in between the balanced outputs can effectively shorten the required coupled line length, which is illustrated in Fig. 2.2.

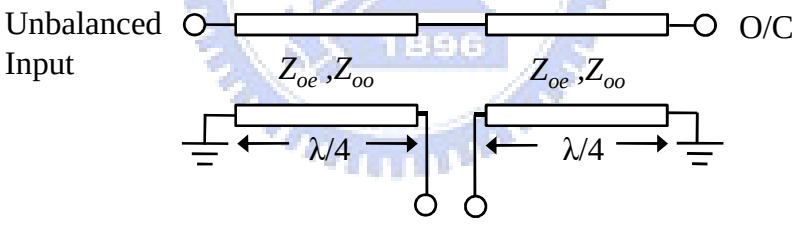

Fig. 2.1. Conventional planar Marchand balun using distributed quarter wavelength coupled lines.

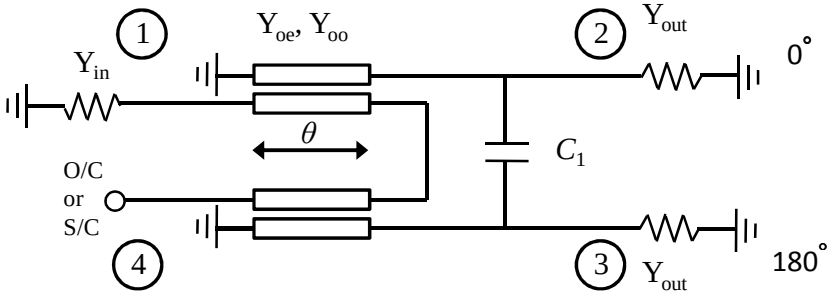

Fig. 2.2. Miniaturized planar Marchand balun with a lumped capacitor connected in between the balanced output ports 2 and 3.

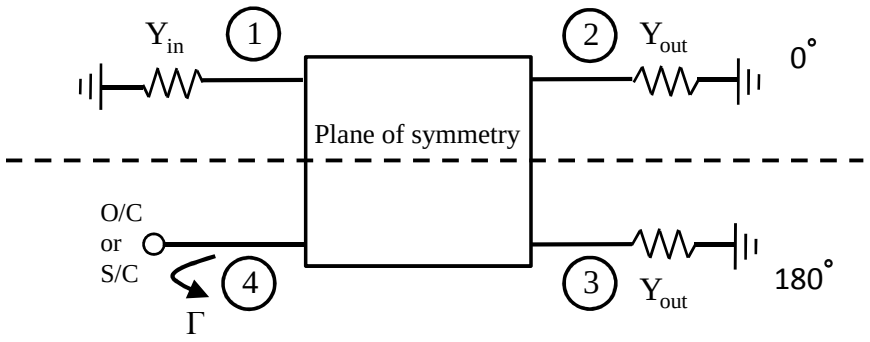

Fig. 2.3. Schematic diagram for the balun configured as a symmetry 4-port network with one port terminated with an open or short circuit.

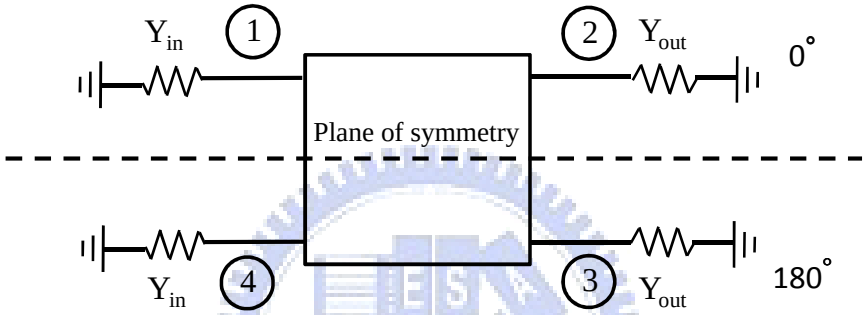

Fig. 2.4. Corresponding symmetry 4-port network for even- and odd-mode analysis.

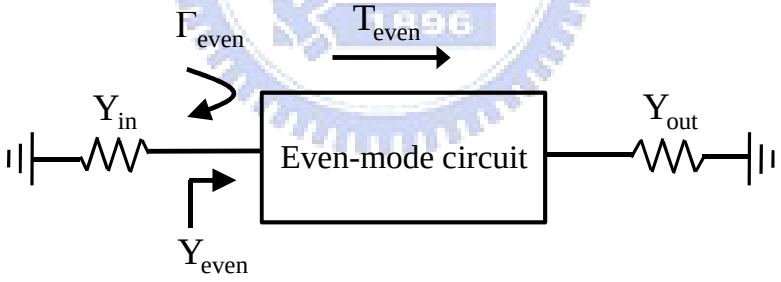

(a)

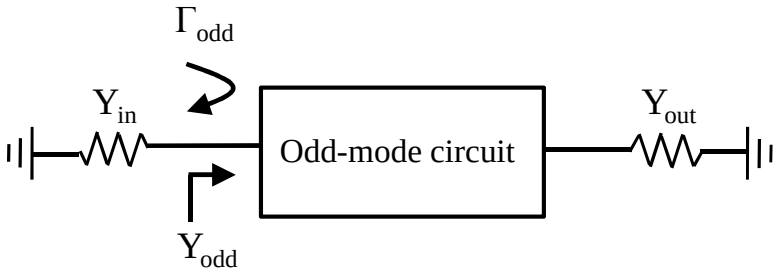

(b)

Fig. 2.5. (a) Even-mode half circuit circuit. (b) Odd-mode half circuit for the symmetry 4-port network in Fig. 2.4.

The miniaturized balun described above can be analyzed through the systematic approach given in [24]. To begin with, the miniaturized Marchand balun is considered as shown in Fig. 2.3, where the symmetry 4-port network with one port terminated with an open or short circuit is depicted. The characteristics of the 3-port balun can be obtained by analyzing the symmetry 4-port network first as illustrated in Fig. 2.4. It is noted that port 4 is terminated with Y_{in} to make the whole structure symmetry. Then, the symmetry 4-port network can be decomposed into even- and odd-mode half circuit for analysis as shown in Fig. 2.5. After some simple computation, the 4-port *S*-matrix can be derived in terms of the even/odd mode reflection (Γ_{even} and Γ_{odd}) and transmission (T_{even}) coefficient. Finally, the 3-port S-matrix for the balun is easily derived from the 4-port *S*-matrix by assigning the boundary condition (Γ) of port 4 as given in Fig. 2.3.

To achieve balun operation, the ports defined in Fig. 2.3 must satisfy the following conditions.

$$S_{11} = 0 \tag{2.1}$$

$$S_{21} = -S_{31} \tag{2.2}$$

Apply these conditions into the previously derived 3-port *S*-matrix. As given in [24],
To satisfy (2.1)

$$\frac{\Gamma_{even} + \Gamma_{odd} - 2\Gamma_{even}\Gamma_{odd}\Gamma}{2 - \Gamma(\Gamma_{even} + \Gamma_{odd})} = 0 \tag{2.3}$$

To satisfy (2.2)

$$\frac{T_{even}(1 - \Gamma_{odd}\Gamma)}{2 - \Gamma(\Gamma_{even} + \Gamma_{odd})} = 0 \tag{2.4}$$

where the notation Γ denotes the reflection coefficient in port 4 as defined in Fig. 2.3.
Assume the denominators in (2.3) and (2.4) are not zero, these equations can be further simplified as follows by replacing Γ_{even} and Γ_{odd} by Y_{even}, Y_{odd}, and Y_{in} defined in Fig. 2.5.

$$T_{even} = 0 \tag{2.5}$$

$$Y_{even} + Y_{odd} = 2Y_{in} \quad \text{for the short-circuit case } \Gamma = -1 \tag{2.6}$$

$$\frac{1}{Y_{even}}+\frac{1}{Y_{odd}}=\frac{2}{Y_{in}} \quad \text{for the open-circuit case } \Gamma = 1 \tag{2.7}$$

Equation (2.5) indicates that, to achieve perfect amplitude and phase, the balun has to present a transmission stop in the even-mode circuit. Moreover, to achieve the input impedance matching, equation (2.6) shows that the sum of the even- and odd-mode admittance must be twice of the source admittance for the short-circuit case. For the open-circuit case, the sum of the even- and odd-mode impedance must be twice of the source impedance as given in (2.7). The equations (2.5)-(2.7) give the valuable insight into the design of the miniaturized balun by analyzing its even- and odd-model half circuits.

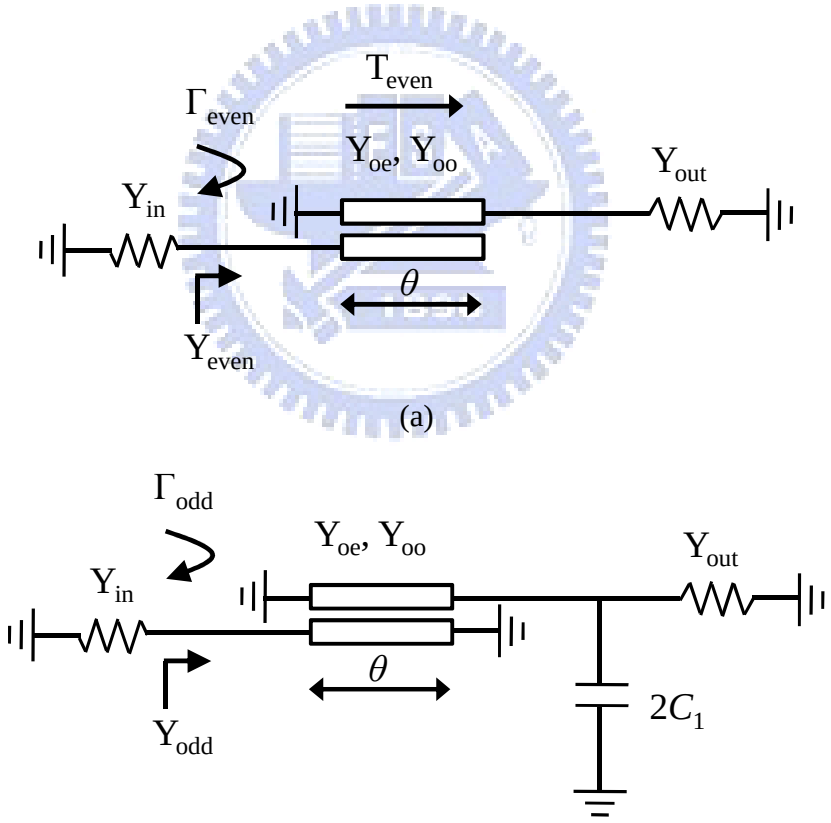

Fig. 2.6. (a) Even-mode circuit. (b) Odd-mode circuit for the miniaturized Marchand balun as shown in Fig. 2.2.

The miniaturized Marchand balun described in Fig. 2.2 is analyzed by the even- and odd-mode circuit shown in Fig. 2.6. It is recognized that the even-mode circuit in Fig. 2.6 (a) presents a perfect transmission stop (T_{even} = 0) that is frequency independent for all values of θ. Thus, equation (2.5) is satisfied automatically. Theoretically perfect and frequency-independent amplitude and phase balance of the miniaturized balun is ensured. To achieve the impedance matching for balun operation, equation (2.6) or (2.7) must be satisfied depending on reflection coefficient Γ of port 4. The even mode and odd mode admittance in Fig. 2.6 can be determined as

$$Y_{\text{even}} = j\frac{(Y_{oe}+Y_{oo})\tan\theta}{2} \tag{2.8}$$

$$Y_{\text{odd}} = Y_{11} - \frac{Y_{12}Y_{21}}{Y_{22}+(j2\omega C_1+Y_{\text{out}})} \tag{2.9}$$

where

$$Y_{11} = Y_{22} = -j\frac{Y_{oo}+Y_{oe}}{2\tan\theta}$$

$$Y_{12} = Y_{21} = -j\frac{Y_{oo}-Y_{oe}}{2\sin\theta}$$

By substituting (2.8) and (2.9) into (2.6) or (2.7) and equating the real and imaging parts, the equations for Y_{oe} and Y_{oo} can be obtained in the following:

$$Y_{oe} = F(\theta, \omega C_1, Y_{\text{in}}, Y_{\text{out}}) = \frac{1}{Z_{oe}} \tag{2.10}$$

$$Y_{oo} = G(\theta, \omega C_1, Y_{\text{in}}, Y_{\text{out}}) = \frac{1}{Z_{oo}} \tag{2.11}$$

Where F and G are functions of θ, ωC_1, Y_{in}, and Y_{out}.

Based on the design equations for Y_{oe} and Y_{oo} in (2.10) and (2.11), different design curves can be obtained. The miniaturized balun can be designed by considering the tradeoffs between the coupled line length, capacitance, bandwidth, and impedance transforming ratio, which is more flexible than conventional Marchand balun.

Chapter 3 DESIGN OF THE SINGLE-BAND CURRENT DRIVER

3.1 GEOMETRY AND CIRCUIT MODEL

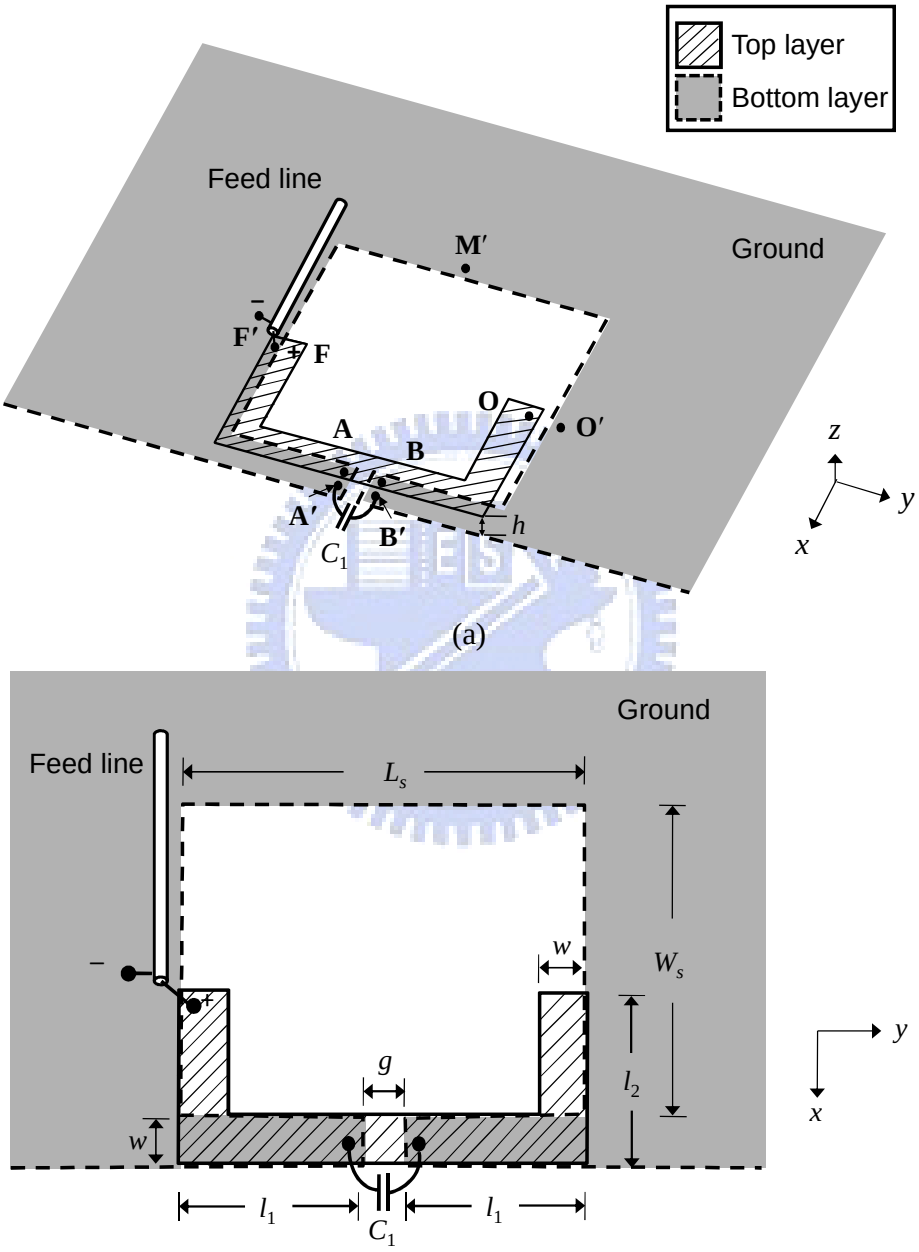

Fig. 3.1. (a) Perspective view of the proposed current driver, where F, A, B, and O points are on the top layer, and F', A', B', O', and M' points are on the bottom layer layer. (b) Configuration of the proposed current driver.

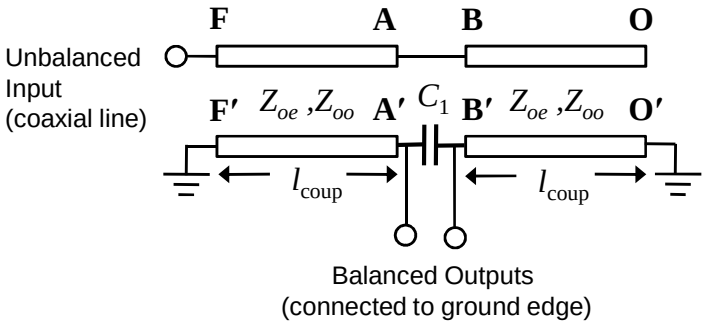

Fig. 3.2. Equivalent circuit model for the proposed current driver.

TABLE II

Detailed dimensions for the proposed current driver

parameter	L_s	W_s	C_1	l_1	l_2	w	g
value	4 mm	3.5 mm	0.4 pF	1.5 mm	2 mm	0.5 mm	1 mm

In this chapter, the proposed current driver is demonstrated at 2.45 GHz for IEEE 802.11 b/g/n WLAN applications. It is fabricated on the ground edge of an FR4 substrate with thickness h = 0.4 mm and dielectric constant ε_r = 4.4. The size of the substrate is $L \times W$ = 50 mm × 100 mm, which is the standard size for PCMCIA applications. Fig. 3.1(a) and Fig. 3.1(b) show the perspective view and top view of the proposed current driver, respectively. The letters in the figure designate the relative position in the equivalent circuit model shown in Fig. 3.2. The current driver lies in the *xy* plane and is printed on both sides of the FR4 substrate. It comprises a U-shaped metal strip with strip width of w on the top layer and a slot of size $L_s \times W_s$ on the bottom layer. The slot is open to the ground edge through a small gap g. A lumped-circuit capacitor C_1 is connected in between points A′ and B′ on the bottom layer. This capacitor here can also be replaced by a printed one. The current driver is fed by a 50 Ω feed line, which can be a coaxial line or a microstrip line. The positive terminal of the feed line is connected to one end of the U-shaped strip (point F) on the top layer, and the negative terminal is connected to the ground point near the slot edge (point F′) on the bottom layer. The overall size of the current driver is only 4 mm × 4mm, which is about 0.03 λ_0 × 0.03 λ_0, with λ_0 being the free-space wavelength at 2.45 GHz.

To explain the operating principle of the current driver, an equivalent circuit model is introduced based on structure observation. It has to be emphasized that this equivalent circuit model is a conceptual model, but not an exact one. In spite of that, the circuit model gives a valuable understanding of the properties of the current driver.

The circuit model is derived as follows: In Fig. 3.1(a), it is noted that the U-shaped metal strip couples to the overlapping slot edge mostly through broadside coupling. Here, a section from points F to A (top layer) and that from F′ and A′ (bottom layer) are considered as a pair of coupled lines. These two coupling transmission lines share the same ground $\overline{\mathrm{F'M'O'}}$ along the slot edge on the bottom layer. The reason they form two coupled lines but not a single transmission line will become clear when the simulated surface current distribution on them are depicted later. Similarly, the parallel sections $\overline{\mathrm{BO}}$ (top layer) and $\overline{\mathrm{B'O'}}$ (bottom layer) form another pair of coupled lines with the same ground $\overline{\mathrm{F'M'O'}}$. The equivalent circuit model can thus be drawn as Fig. 3.2, which is actually a miniaturized planar balun similar to a conventional planar Marchand balun [26, 27], but with difference in the capacitor C_1 between the balanced outputs (points A′ and B′) for size reduction [24]. Because the current driver has a function like a balun, it can generate differential signals at the two ends of the capacitor so the in-phase ground edge currents could be induced. The total radiation is mainly attributed to these induced ground edge currents.

The miniaturized planar balun with a lumped-circuit capacitor shows more degrees of freedom in design than the conventional planar marchand balun does. It can be implemented by a wide range of practical values for even-mode impedance Z_{0e} and odd-mode impedance Z_{0o} depending on various values of C_1 with different lengths of coupled lines. Moreover, this miniaturized balun structure is theoretically perfect and frequency independent with amplitude and phase balances. Several important characteristics of the miniaturized planar balun that are beneficial to the design of the current driver are listed in the following:

a). The required value of Z_{0e} for the balun increases with decreasing coupled line length l_{coup}.

b). The required value of Z_{0e} for the balun decreases when the capacitance C_1 increases.

c). The required value of Z_{0o} is not sensitive to the coupled line length or the capacitance

C_1.

d). For a fixed coupled line length, the balun with larger Z_{0e} and smaller C_1 exhibits wider bandwidth.

From characteristics *a*) and *b*), it shows that the balun size can be reduced with large C_1 while Z_{0e} is remained fixed. However, characteristic *d*) indicates the balun with larger Z_{0e} exhibits wider bandwidth, so C_1 and Z_{0e} are appropriately chosen depending on desired bandwidth.

The proposed current driver is designed similar to the miniaturized balun. The even-mode impedance Z_{0e} of the current driver is determined by the slot width W_s, which is related to the equivalent distance between coupled lines and ground plane. Thus, Z_{0e} increases with larger slot width W_s. The coupling strength between the coupled lines is affected by the strip width *w*, so odd-mode impedance Z_{0o} is related to the strip width *w*. A larger strip width *w* corresponds to a lower value of the odd-mode impedance. Also, as stated in *d*), the bandwidth increases when Z_{0e} increases, and thus the larger slot size for the current driver. Therefore, bandwidth and size are tradeoffs.

3-2 SINGLE-BAND CURRENT DRIVER DESIGN

As stated, the current driver can be considered as a miniaturized balun, which is characterized by the even-mode impedance Z_{0e}, the odd-mode impedance Z_{0o}, the length of the coupled lines l_{coup}, and the capacitor in the circuit model. In this section, the current driver is investigated through the simulated results of the return losses and total gains on the *z* axis for these parameters. Without the specification, the other parameters of the simulation are the same as given in TABLE II. The simulation results are obtained using Ansoft High Frequency Structure Simulator (HFSS) [28]. The FR4 substrate loss is considered in the simulation with the loss tangent of 0.02.

Fig. 3.3 shows the simulated return losses and gains on the *z* axis for the current driver with various capacitances C_1. It is observed that the center frequency is shifted downwards with increasing C_1, from 2.73 GHz to 2.27 GHz as C_1 varies from 0.3 pF to 0.5 pF. This trend of the return losses agrees with characteristics *a*) and *b*) of the miniaturized balun, which indicate the capacitor C_1 is used for size reduction. Good impedance matching is also maintained with various C_1, so the center frequency of the

current driver can be easily adjusted by varying C_1 with little influence on impedance matching. Furthermore, the peak gain on the *z* axis keeps a value near 0 dBi, not changed much due to the variation of C_1. The variations of gain over the 10-dB impedance bandwidth of the current driver for C_1 = 0.3 pF, 0.4 pF, and 0.5 pF are 0.66 dBi, 0.5 dBi, and 0.4 dBi, respectively. This suggests that the ground edge currents induced by the current driver maintain good radiation property despite the change of C_1, and thus the center frequency.

The slot width *W*s is a crucial parameter related to the even-mode impedance of the coupled lines in the equivalent model. Characteristic *a*) of the miniaturized balun shows the required value of Z_{0e} increases with decreasing coupled line length. Thus, the operating frequency moves downwards when the slot width W_s increases. Fig. 3.4 illustrates the simulated return losses and gains on the *z* axis with W_s equal to 3 mm, 3.5 mm, and 4 mm. As seen in the figure, the center frequency is shifted downwards from 2.59 GHz to 2.36 GHz as the slot width W_s increases from 3 mm to 4 mm. In the meanwhile, the peak gain at the center frequency remains nearly unchanged. It is worth noting that both C_1 and W_s can be used to adjust the operating frequency of the current driver with negligible effect on the impedance matching.

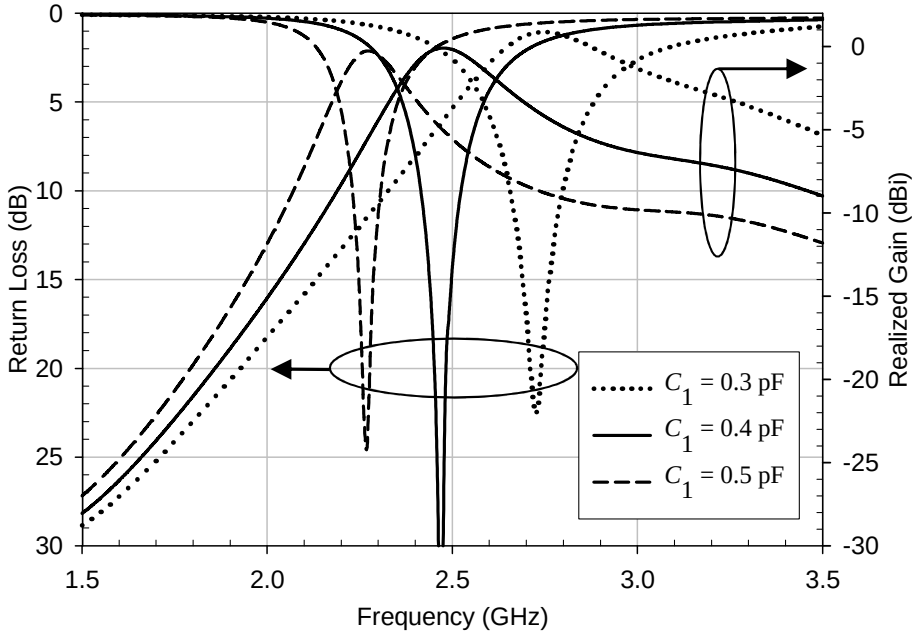

Fig. 3.3. Simulated return loss and total gains on the *z* axis for the proposed current driver as a function of C_1.

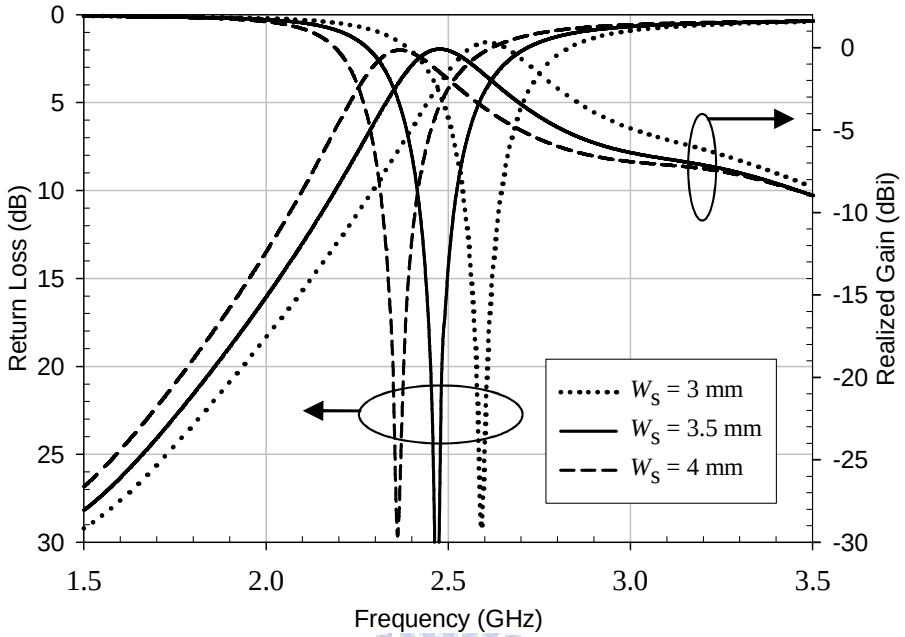

Fig. 3.4. Simulated return loss and total gains on the *z* axis for the proposed current driver as a function of slot width, W_s.

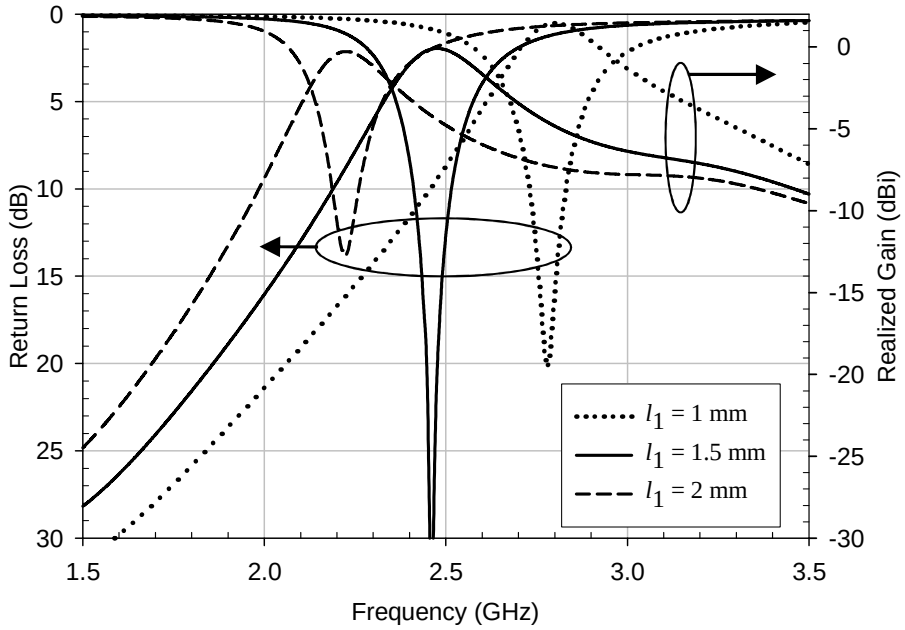

Fig. 3.5. Simulated return loss and total gains on the *z* axis for the proposed current driver as a function of l_1. It is noted here slot length L_s varies with l_1 ($L_s = 2l_1 + g$).

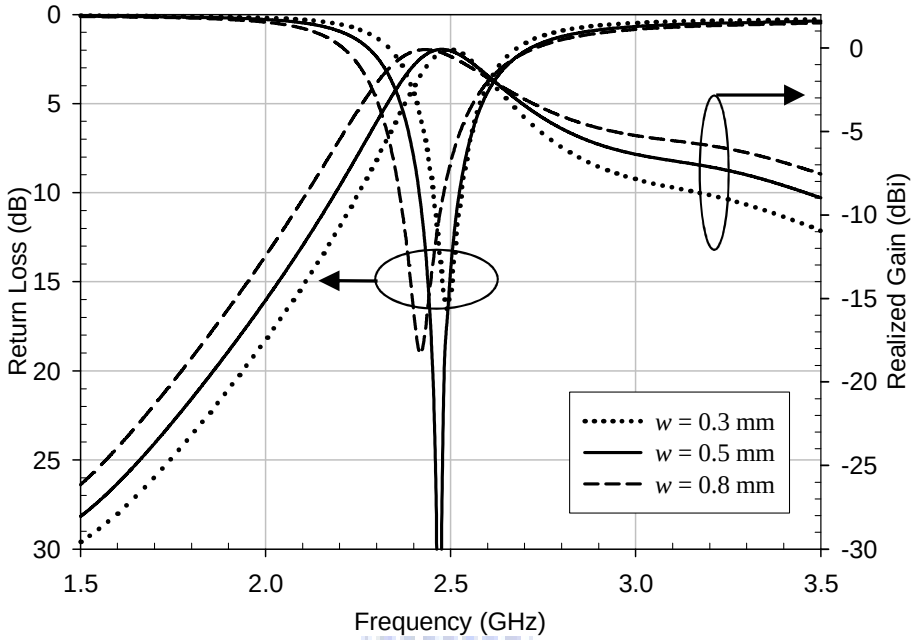

Fig. 3.6. Simulated return loss and total gains on the *z* axis for the proposed current driver as a function of strip width, *w*.

In the proposed current driver, the coupled lines are bent into two sections l_1 and l_2 for size reduction. The effect of the length of coupled lines is examined by adjusting l_1 while l_2 is fixed to 1.5 mm. Fig. 3.5 depicts the return loss and gains on the *z* axis for various strip length l_1 (1 mm, 1.5 mm, and 2 mm). Obviously, the center frequency moves lower with larger l_1. As l_1 increases from 1mm to 2 mm, the center frequency decreases from 2.78 GHz to 2.22 GHz. Notice that the peak gain on the *z* axis for various l_1 is quite stable.

Fig. 3.6 shows the effect on return loss and gains on the *z* axis for various strip width *w* (0.3 mm, 0.5 mm, and 0.8 mm). There is a slight frequency shift shown in the figure with varying *w*. The strip width is related to the coupling coefficient of the coupled lines, especially in l_1 section. In addition, the strip width has a dominant effect on Z_{0o} but a subtle effect on Z_{0e}. Since the required value of Z_{0o} is less sensitive to the coupled line length (characteristic *c*). Thus, the change of strip width *w* would not lead to large frequency shift as expected.

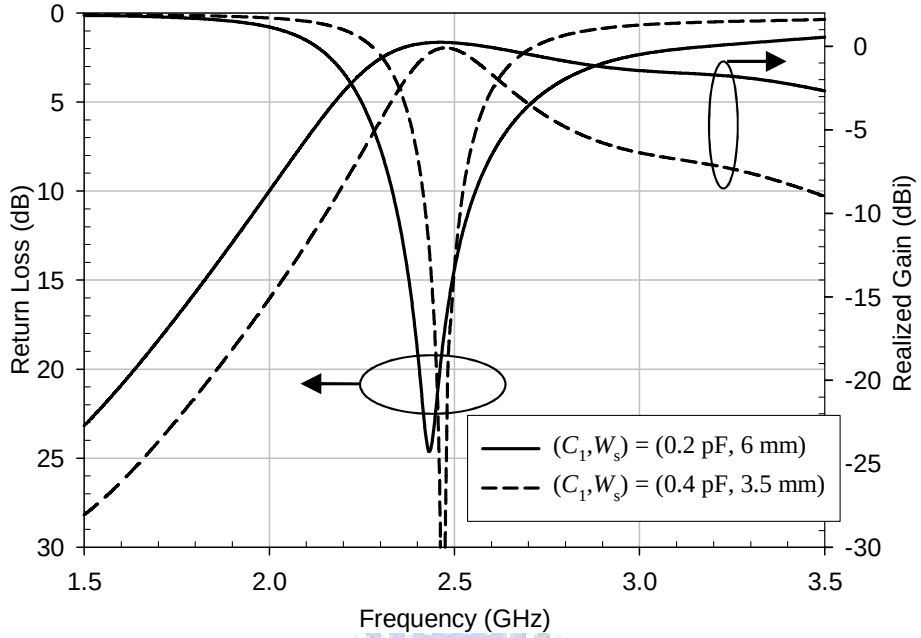

Fig. 3.7. Simulated return loss and total gains on the *z* axis for the proposed current driver with two configurations (C_1 = 0.2 pF, W_s = 6 mm) and (C_1 = 0.4 pF, W_s = 3.5 mm). Other structure parameters of the current driver (C_1 = 0.2 pF, W_s = 6 mm) are L_s = 4 mm, l_1 = 1.5 mm, l_2 = 3 mm, and w = 0.5 mm. Other parameters of the current driver (C_1 = 0.4 pF, W_s = 3.5 mm) are the same as given in TABLE II.

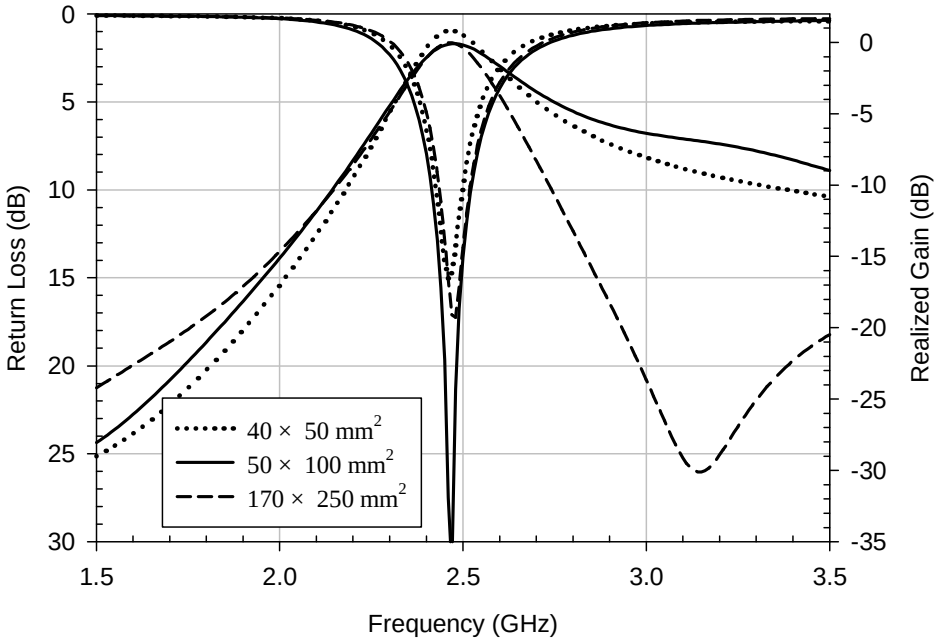

Fig. 3.8. Simulated return loss and total gains on the *z* axis for the proposed current driver with ground sizes $L \times W = 40 \times 50$ mm^2, 50×100 mm^2, and 170×250 mm^2. The current driver is placed in the center of the ground edge *L*.

According to characteristic *d*) of the miniaturized balun, the balun with larger Z_{0e} and smaller C_1 exhibits wider bandwidth. This property is illustrated in Fig. 3.7, which shows the return loss and gains on the *z* axis for two sets of C_1 and the corresponding slot width W_s (C_1 = 0.4 pF, W_s = 3.5 mm and C_1 = 0.2 pF, W_s = 6 mm). The 10-dB return loss bandwidth changes from 120 MHz (2.40 GHz to 2.52 GHz) to 230 MHz (2.33 GHz to 2.56 GHz) as C_1 varies from 0.4 pF (W_s = 3.5 mm) to 0.2 pF (W_s = 6 mm). The cost of bandwidth enhancement for the current driver is a larger slot size. Thus, the current driver can be designed flexibly for various requirements of bandwidth. In this study, the current driver is designed for 2.45 GHz IEEE 802.11 b/g/n WLAN applications. The bandwidth of the current driver with C_1 = 0.4 pF and W_s = 3.5 mm is adequate for the specification.

After the discussion on the effects of the structure parameters and the capacitor C_1 on the current driver, it is necessary to investigate the sensitivity of the antenna performance to ground size. Fig. 3.8 shows that the return loss for various ground sizes, $L \times W$ = 40 × 50 mm^2, 50 × 100 mm^2, and 170 × 250 mm^2. It is seen that the ground size has minor effect on the return loss for the current driver. The center frequency is almost unchanged with different ground sizes. The gains on the *z* axis are also shown in the figure. As observed, the peak gains and gain variations in the 10-dB return-loss bandwidth are about the same. The rapid gain variation in the higher outband for the ground size of 170 × 250 mm^2 is due to the high-order-mode current distribution along the edge.

3-3 SHIELDING BOX EFFECT

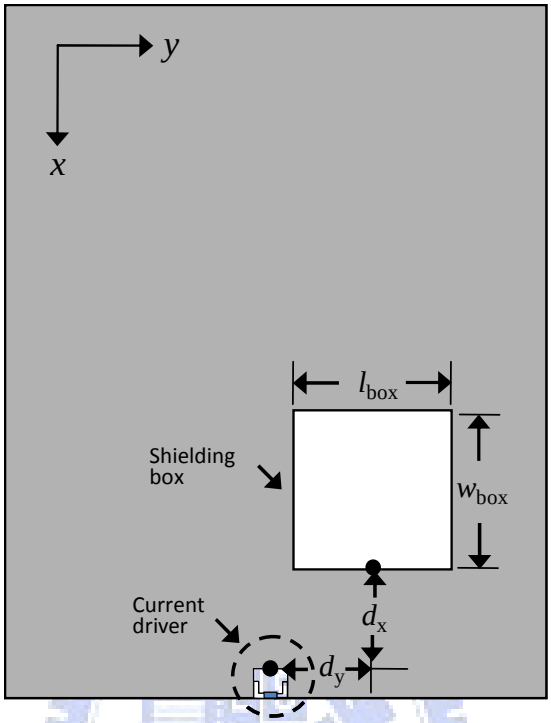

Fig. 3.9. Configuration of the current driver and the shielding box.

As shown previously, the design trend of the hand-held devices is compactness for better mobility. However, in addition to the antenna miniaturization, EMI (Electromagnetic Interference) is also important when all devices are fabricated on a small circuit board. It is common to address EMI problems by covering the RF circuitry with a shielding metal box to isolate it from the interference. Due to the skin effect, the outside current cannot penetrate into the inside of the shielding box. Although there are openings on the shielding box for the signals to come in and out, the shielding box can still functions well because the size of the openings is very small compared to the wavelength of the operating frequency. In this section, we will simulate the effect of the shielding box on the current driver as a function of the position and size of the shielding box. The simulation is conducted by ANSOFT HFSS. Finally, the result of the current driver with the shielding box is compared with the previous result without the shielding box, and the shielding box effect can be easily addressed by adjusting the structure parameter slot width W_S.

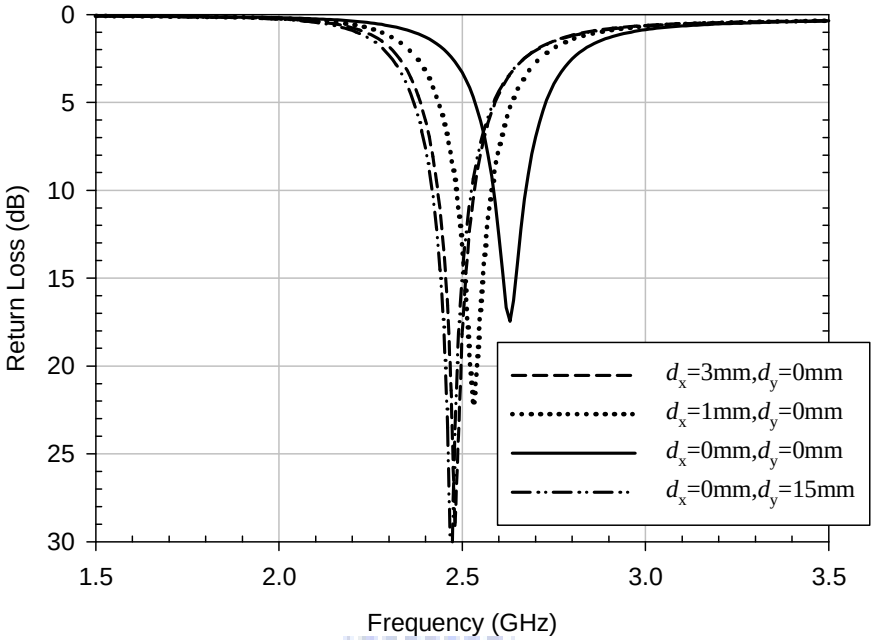

(a)

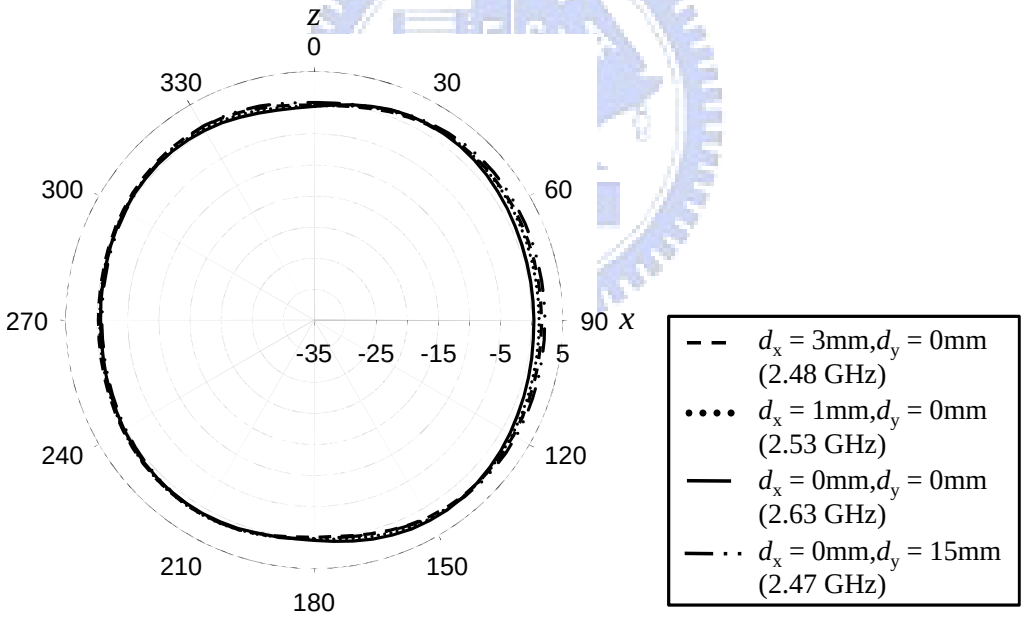

(b)

Fig. 3.10. (a) Simulated return loss for the proposed current driver with the shielding box of different positions. (b) Simulated total radiation field patterns in *xz* plane for the current driver with shielding box of different positions. The size of the shielding box is $20 \times 20 \times 2$ mm^3. The parameters of the current driver are the same as given in TABLE II.

The effect of the shielding box on the current driver is investigated. As shown in Fig. 3.9, the shielding box is placed on the top layer with surrounding shorting poins connected to the ground plane through the substrate. The geometrical parameters of the shielding box are length l_{box}, width w_{box}, and height h_{box} (+z direction). The distance between the shielding box and the current driver is decomposed into two components, vertical component d_x and horizontal component d_y. Fig. 3.10 helps to understand the effect of the shielding box on the return loss and gains of the current driver when the shielding box is placed at different positions. The size of the shielding box is $l_{box} \times w_{box} \times h_{box} = 20 \times 20 \times 2$ mm^3. As seen in Fig. 3.10(a), the frequency responses of the return loss have similar behaviors for d_x = 3, 1, and 0 mm (with d_y fixed at 0 mm). The center frequency is slightly shifted from 2.48 to 2.63 GHz. The more the shielding box is moved toward the current driver, the higher is the center frequency. Only 6% frequency shift is observed even when the shielding box is put directly above the current driver (i.e., $d_x = d_y = 0$ mm). As will be seen later, this slight frequency shift can be easily restored by tuning the driver's structure parameter. Although not shown here, the shielding box has negligible effect on the current driver when the vertical distance is more than 3 mm. Also, since the induced current is concentrated on the ground edge for radiation, the effect of the shielding box placed along the edge is also considered. The fourth curve in Fig. 3.10(a), d_x = 0 mm and d_y = 15 mm, represents the return loss when the shielding box is aligned with the right side of the ground edge. The response is almost identical to that of a stand-alone current driver, which means that the proximity shielding box has no obvious effect on the current driver.

Fig. 3.10(b) shows the simulated total radiation field patterns in xz plane for the current driver with the shielding box at different positions. The radiation patterns are omni-directional and almost the same with average gains varying between 0.65 dBi and 1.04 dBi. This implies that the existence of the nearby shielding box has little influence both on the return loss response and the radiation performance of the current driver.

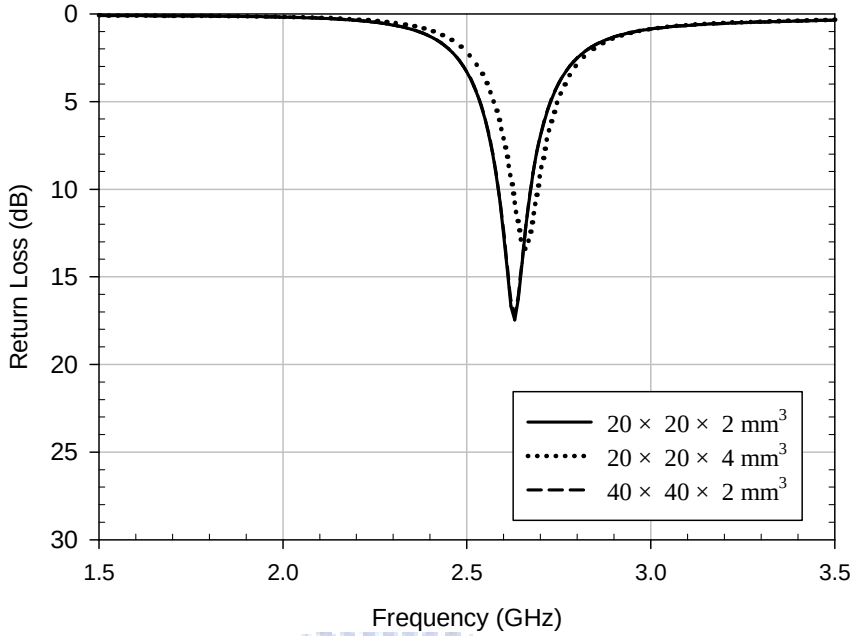

Fig. 3.11. Simulated return loss for the proposed current driver with shielding box of different sizes. The shielding box is aligned with the slot edge of the current driver (d_x = 0 mm and d_y = 0 mm). The parameters of the current driver are the same as given in TABLE II.

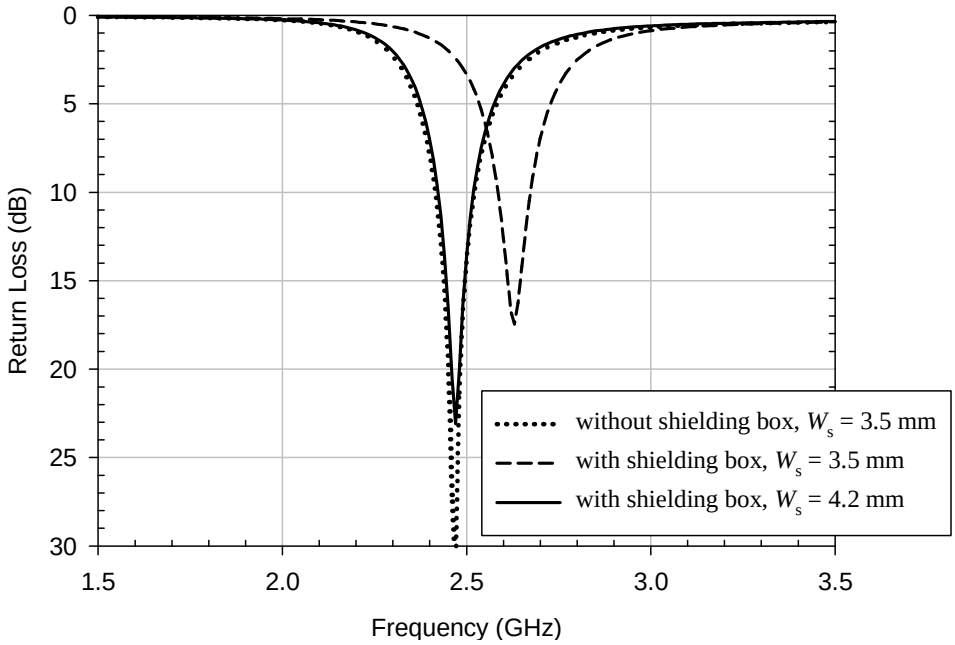

Fig. 3.12. Simulated return loss for the proposed current driver with and without the presence of the shielding box. The shielding box is placed directly above the current driver (d_x = 0 mm and d_y = 0 mm) with the size of 20 × 20 × 2 mm^3. The parameters of the current driver are the same as given in TABLE II.

The influence of the shielding box volume is examined in Fig. 3.11, which shows the return loss of the current driver for various sizes of the shielding box. It can be seen that the return loss is nearly not affected by the width and height of the shielding box. The return loss curve for the 20 mm × 20 mm × 2 mm shielding box is almost overlapped with the curve for the 40 mm × 40 mm × 2mm one. Furthermore, by comparing the first curve (20 mm × 20 mm × 2 mm) and the second curve (20 mm × 20 mm × 4 mm), the center frequency moves from 2.63 GHz to 2.65 GHz as h_{box} varies from 2 mm to 4 mm. This variation shows that the height of the shielding box has minor effect on the return loss.

From the above discussion, the vertical distance d_x of the shielding box is the most important factor that determines the amount of frequency shift. However, even in the worst cast that the shielding box is placed directly above the current driver (i.e., $d_x = d_y =$ 0 mm), the frequency shift can be easily resumed by slightly adjusting the current driver's dimension. To demonstrate this, Fig. 3.12 shows the simulated return loss with and without the presence of a shielding box. The dotted line indicates the frequency response of the original design (with slot size of $L_s \times W_s = 4 \times 3.5$ mm^2) without the proximity shielding box, which shows a design frequency at 2.47 GHz. After putting the shielding box of size 20 mm × 20 mm × 2 mm directly above the current driver ($d_x = d_y =$ 0 mm), the response turns out to be the dashed line, where the center frequency is now shifted to 2.63 GHz. To tune the frequency into the design one, we simply increase the slot width W_s of the current driver from 3.5 mm to 4.2 mm. The increase of the slot width would decrease the center frequency (as shown in Fig. 3.4), so that the resultant frequency response (solid line) resumes to the design one.

3-4 SINGLE-BAND CURRENT DRIVER DESIGN WITH A PRINTED CAPACITOR

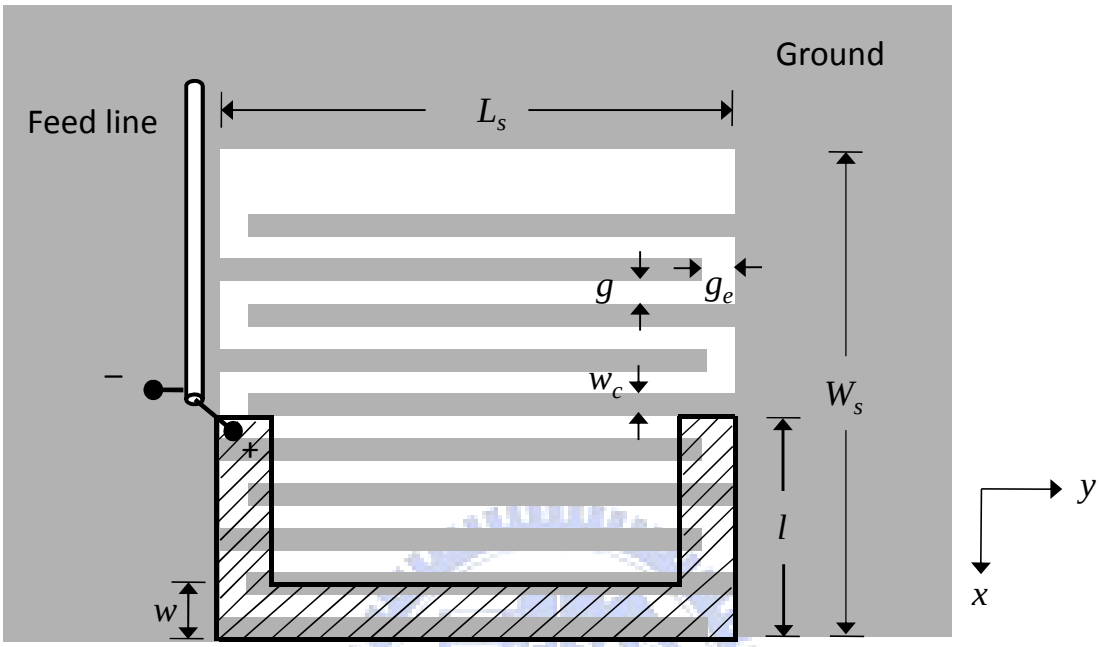

Fig. 3.13. Configuration of the proposed current driver with a printed interdigital capacitor.

TABLE III

Detailed dimensions for the proposed current driver with a printed capacitor

parameter	L_s	W_s	N_1	l	w	$g = g_e$	w_c
value	4 mm	4 mm	10	2 mm	0.5 mm	0.2 mm	0.2 mm

As demonstrated previously, the center frequency of the current driver is very sensitive to the capacitance. However, the lumped capacitor inevitably has the fabrication inaccuracy. This may cause problem, especially for narrow band applications. Also, using lumped capacitor in the design will increase the fabrication cost. To reduce the cost and increase the design flexibilities, the current driver for 2.4 GHz WLAN applications is redesigned with another configuration by replacing the lumped capacitor with the printed one as shown in Fig. 3.13. In the figure, the current driver lies in the *xy* plane and is printed on both sides of the FR4 substrate. It comprises a U-shaped metal strip with strip width of w on the top layer and a slot of size $L_s \times W_s$ on the bottom layer. Inside the slot

are filled with a printed interdigital capacitor. The interdigital capacitor is defined by the figure width w_c, the gap between figures g, the gap at the end of the fingers g_e, and figure number N. The finger length varies with the slot length L_s. Also, the U-shaped metal strip is aligned with slot edge, and has two arms of the length l. The whole size of the current driver is determined by the slot size $L_s \times W_s$. The current driver is fed by a 50 Ω transmission line, which can be a coaxial line or a microstrip line with the positive terminal connected to one arm of the U-shaped metal strip and the negative terminal connected to the ground plane near the slot edge. The driver, which is located in the center of the shorter ground edge, is fabricated on an FR4 substrate of 50 mm × 100 mm with thickness h = 0.4 mm and dielectric constant ε_r = 4.4.

The design of the current driver with a printed capacitor is basically the same as those described above for the current driver with a lumped capacitor. The center frequency is determined by the slot size $L_s \times W_s$ and the capacitance. Moreover, the input impedance is easy to be matched at 50 Ω with appropriate coupling strength, which is controlled by the strip width w and arm length l_1 of the U-shaped metal strip on the top layer. Detailed dimensions for the current driver are listed in TABLE III. It is noticed that the overall size for the current driver with a printed capacitor remains the same as the size for the current driver with lumped capacitor.

The performance of the two configurations for the current driver is compared in Fig. 3.14, which shows the frequency response of the return loss for the current driver with the printed capacitor and lumped capacitor. It is observed in the figure that the two curves are almost overlapped with each other at 2.45 GHz. This reveals that the overall performance of the current driver is not changed with the lumped capacitor replaced with a printed one. However, the printed capacitor is easy to generate unwanted resonance in the higher frequency, which is not able to induce radiating ground edge for radiation. The additional return loss deep at 5.9 GHz is observed in the figure, which is purely generated by the structure of current driver itself and is basically irrelevant to the ground edge current. Thus, the radiation property is very poor. Although not shown here, the simulated total radiation efficiency is only about 10 %.

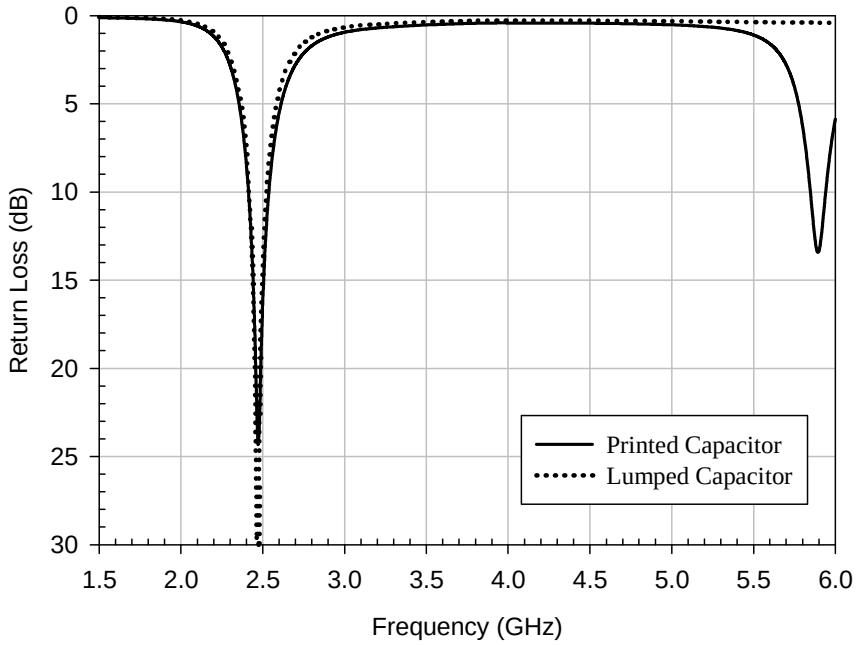

Fig. 3.14. Simulated return loss for the current driver with a printed interdigital capacitor and the lumped capacitor. The parameters for the two current drivers are given in TABLE II and III, respectively.

3-5 MEASUREMENT AND DISCUSSION

3-5-1 Current driver with a lumped capacitor

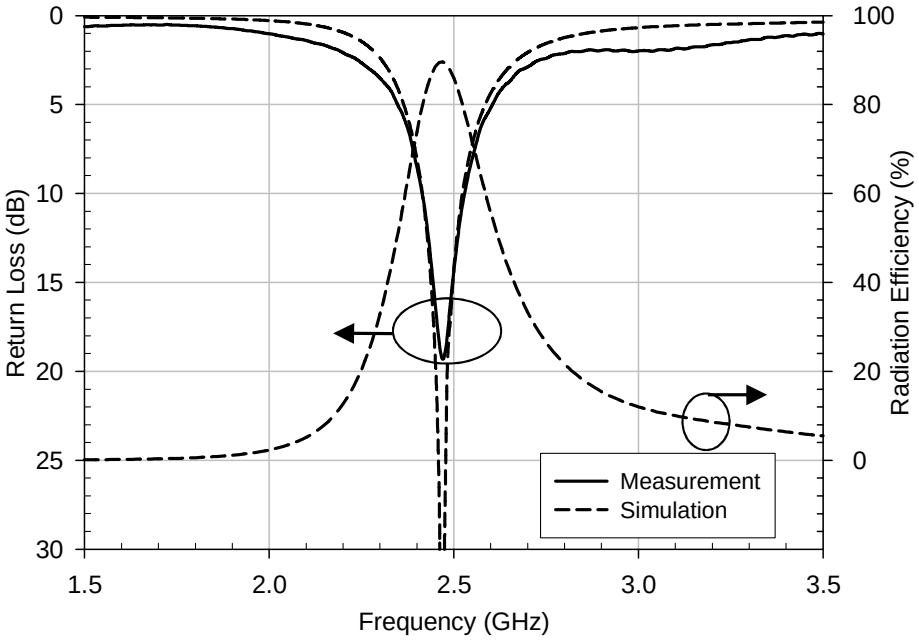

Fig. 3.15. Simulated return loss and radiation efficiency as well as measured return loss for the proposed current driver with a lumped capacitor. The simulated radiation efficiency includes the mismatch loss. The parameters for the current driver are the same as given in TABLE II.

In this section, the measurement results and the corresponding discussion for the proposed current driver fabricated on the ground plane of 50×100 mm^2 are presented. Fig. 3.15 shows the simulated return loss and radiation efficiency as well as the measured return loss for the proposed current driver with a lumped capacitor. As seen in the figure, the simulated and measured results come to a great agreement. The measured return loss shows 120 MHz 10-dB return-loss bandwidth centered at 2.46 GHz. In addition, over the bandwidth for IEEE 2.4 GHz WLAN operation, the radiation efficiency varies slowly from 74% to 86%.

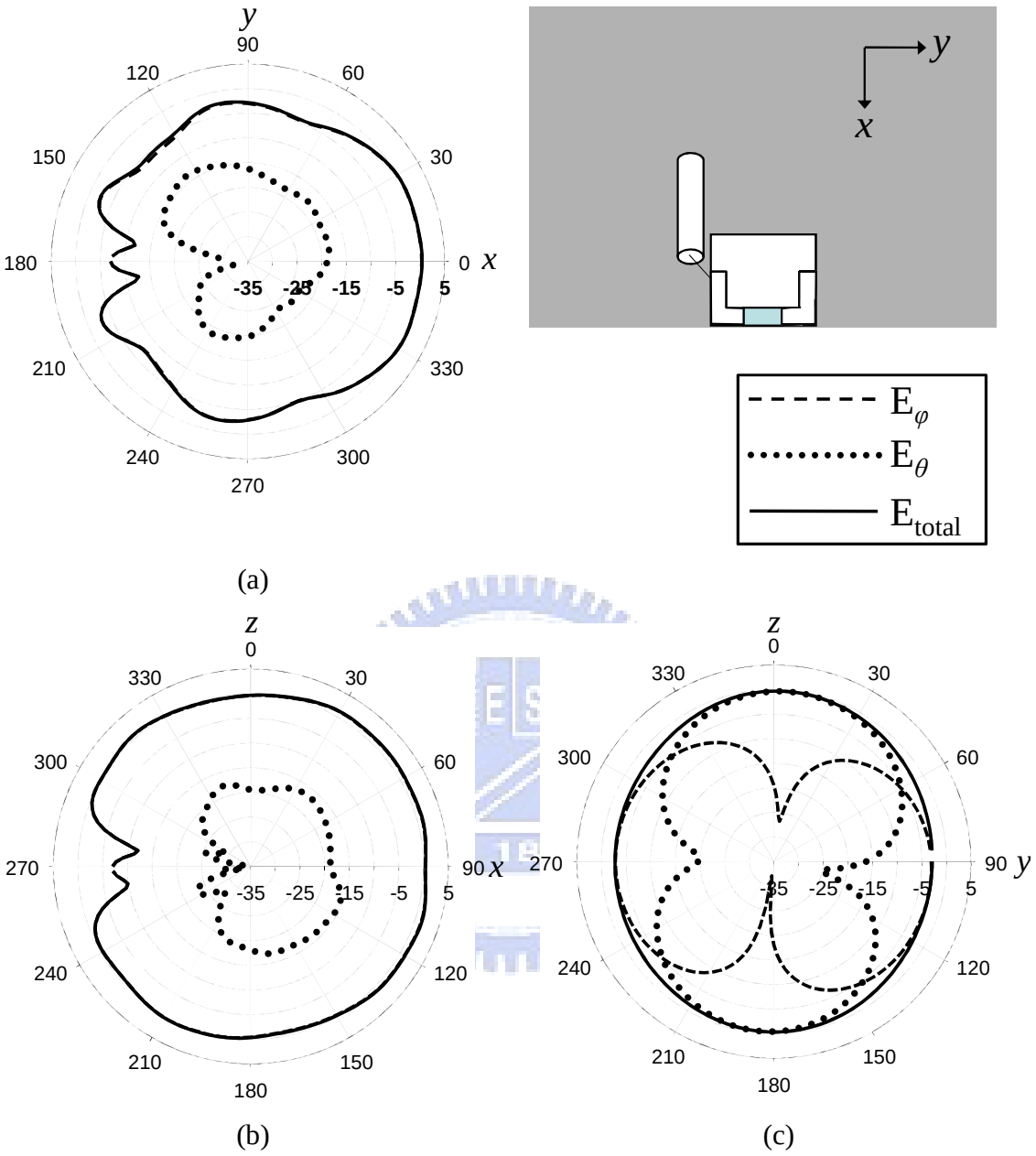

Fig. 3.16. Measured 2-D radiation patterns for the proposed current driver with a lumped capacitor at 2.45 GHz. The driver is fabricated on the ground plane of 50 mm by 100 mm. (a) *xy* plane. (b) *xz* plane. (c) *yz* plane.

TABLE IV

MEASURED GAINS AT 2.45 GHZ FOR THE CURRENT DRIVER WITH A LUMPED CAPACITOR

2.45 GHz	*xy* plane	*xz* plane	*yz* plane
Peak gain (dBi)	0.44	1.20	-0.36
Average gain (dBi)	-2.65	-0.07	-1.67

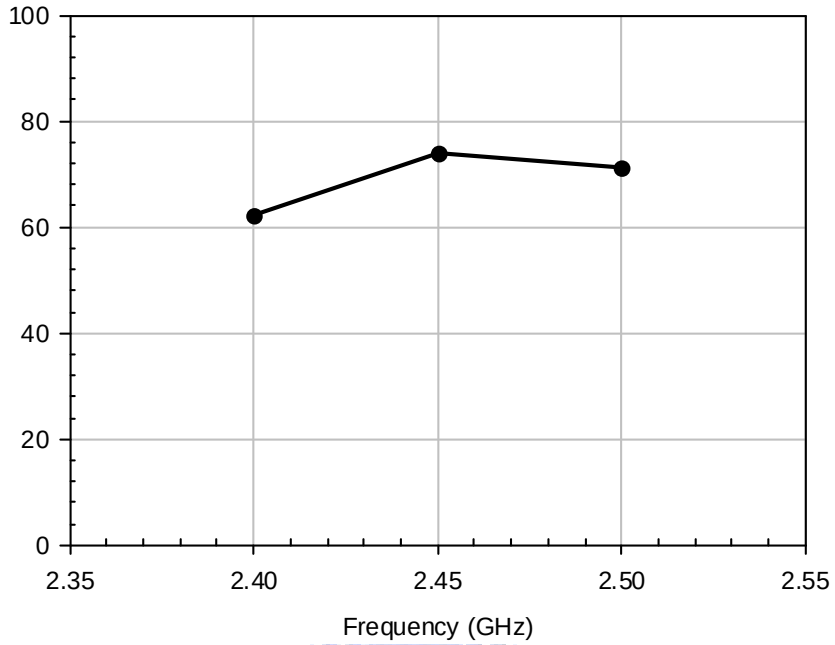

Fig. 3.17. Measured radiation efficiency for the current driver with a lumped capacitor.

The measured radiation patterns at 2.45 GHz in the three principal planes are illustrated in Fig. 3.16. There are generally no nulls for the total-power radiation patterns E_{total} observed in the three principal planes. This omni-directional property makes the proposed current driver promising for many applications. The corresponding values of measured peak and average gains in three principal planes are listed in TABLE IV. About 0 dBi average gain is obtained in the nearly omin-directional pattern in *xz* plane. Also, the measured antenna radiation efficiency is given in Fig. 3.17, where the efficiency varies from 62% to 74% over the band for 2.4 GHz WLAN application. It is noticed that about 10% efficiency difference between the simulated and measured results is observed. This is because that the ohmic loss caused by the cable and the lumped capacitor is not considered in the simulation. The radiation properties of the current driver are quite good, as compared to general printed antennas fabricated on the same substrate.

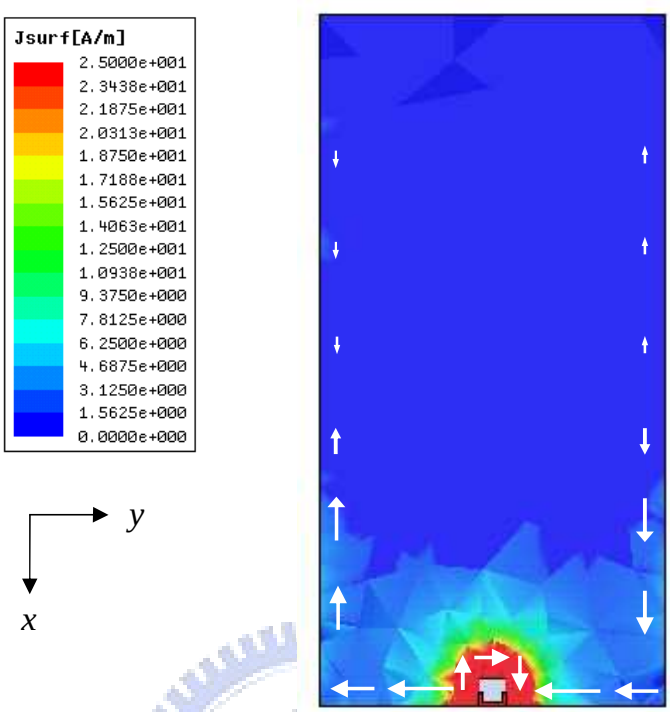

Fig. 3.18. Simulated surface current distribution for the proposed current driver at 2.45 GHz.

To further understand the radiation mechanism, Fig. 3.18 shows the simulated surface current distribution for the current driver at 2.45 GHz. One can observe that the radiating ground edge currents induced by the current driver can be decomposed into two parts: the out-of-phase *x*-direction currents and the in-phase *y*-direction currents. Notice that the out-of-phase *x*-direction currents spaced by near half wavelength in free space produce maximum radiation fields in ± *y* directions but null fields in ± *z* directions. Thus, a digit "8" radiation pattern for the E_{φ} component is obtained in the *yz* plane as shown in Fig. 3.16 (c). In the *xz* plane, the inverted *x*-direction currents cancel each other in the far field, so the radiation pattern for the E_{θ} component is small. Moreover, the in-phase *y*-direction currents are responsible for the omni-directional radiation patterns for the E_{φ} component in the *xz* plane and form a digit "8" radiation pattern for the E_{θ} component in the *yz* plane. The current distribution is consistent with the measured radiation pattern shown in Fig. 3.16. This implies that the main radiation source comes from the current along the ground edge.

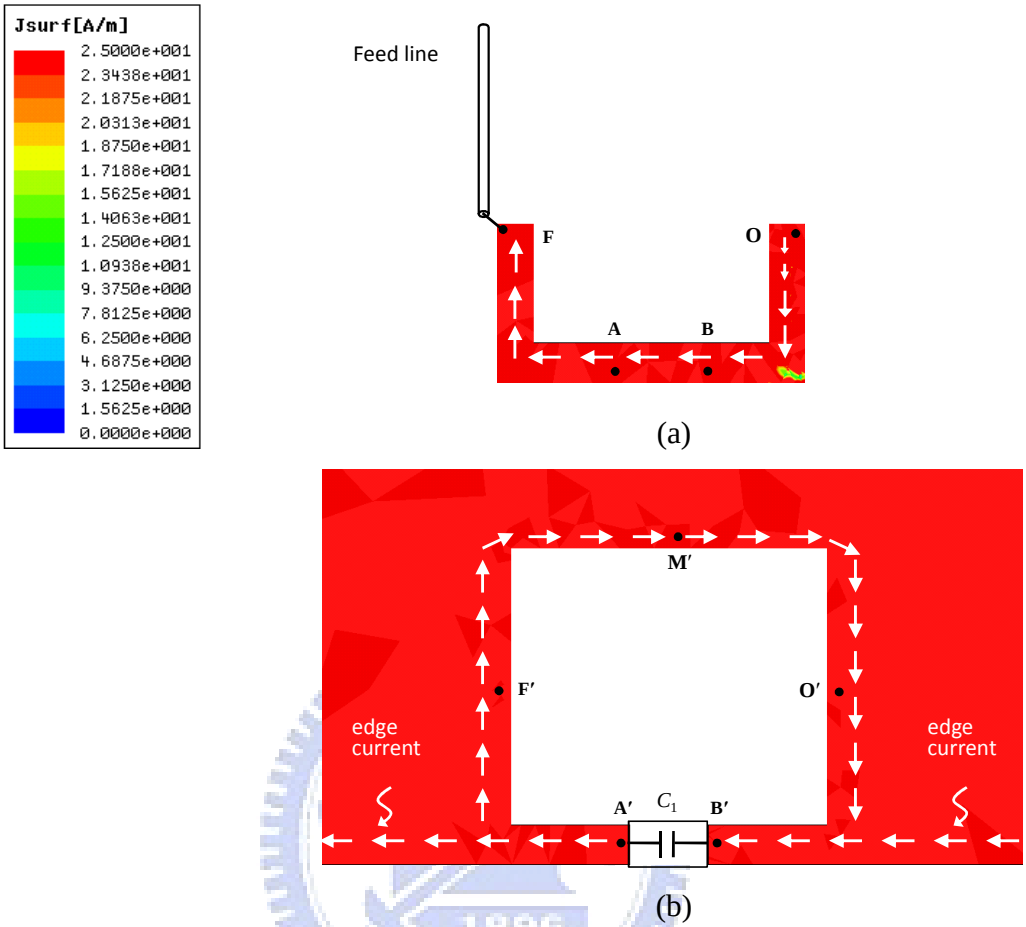

Fig. 3.19. Close view of the simulated current distribution for the proposed current driver at 2.45 GHz. (a) Top view. (b) Bottom view.

The close view of the surface current distribution in the current driver is depicted in Fig. 3.19 Although there are strong currents concentrated in the structure, the currents have little contribution to radiation since the size of the current driver is far smaller than the ground plane. In addition, the radiation from the current on the current driver cancels each other in the far field. Therefore, it shows again that the main radiation is contributed by the ground edge current. As mentioned in Section 3-1, the parallel sections $\overline{FA}$ and $\overline{F'A'}$ form coupled lines instead of a single transmission line. This can be verified from the current distribution illustrated in Fig. 3.19, which shows the currents on the two parallel sections flow in the same direction. It is also true for the currents on the parallel section $\overline{BO}$ and $\overline{B'O'}$. The photograph of the fabricated current driver with a lumped capacitor is shown in Fig. 3.20.

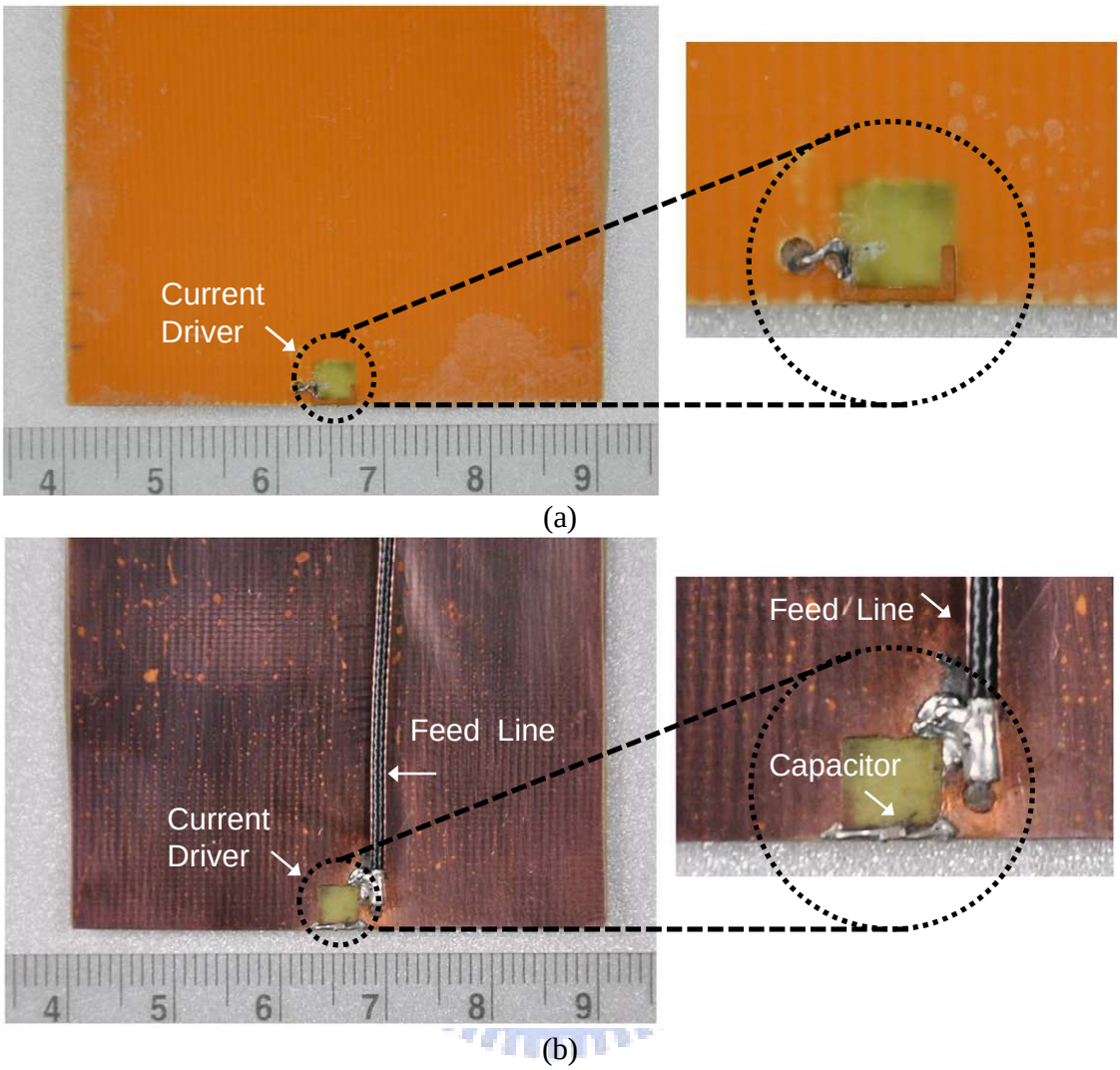

Fig. 3.20. Photograph of the fabrication for the proposed current driver with a connected ground plane of 50 mm × 100 mm. (a) Top view. (b) Bottom view.

3-5-2 Current driver with a printed capacitor

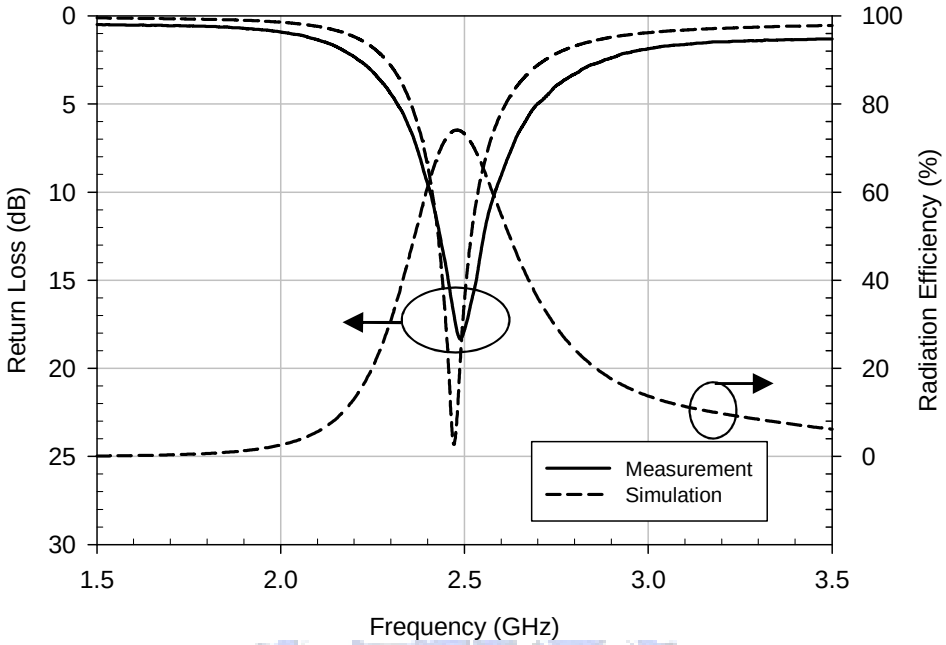

Fig. 3.21. Simulated return loss and radiation efficiency as well as measured return loss for the proposed current driver with a printed interdigital capacitor. The simulated radiation efficiency includes the mismatch loss. All parameters for the current driver are the same as given in TABLE III.

The simulated return loss and radiation efficiency as well as the measured return loss for the proposed current driver with a printed interdigital capacitor are depicted in Fig. 3.21. The size of the ground plane is 50×100 mm^2. As seen in the figure, the simulated return loss generally agrees with the measured one. The measured return loss shows a wider bandwidth than the simulation predicts. The 10-dB return-loss bandwidth is about 180 MHz with the center frequency occurs at 2.48 GHz, which covers the required band for WLAN 2.4 GHz. Moreover, the simulated radiation efficiency varies from 61% to 74%, which agrees well with the measured one, as will be shown later. Compare the simulated radiation efficiency in Fig. 3.15. It suggested that the main ohmic loss for the current driver come from the printed capacitor.

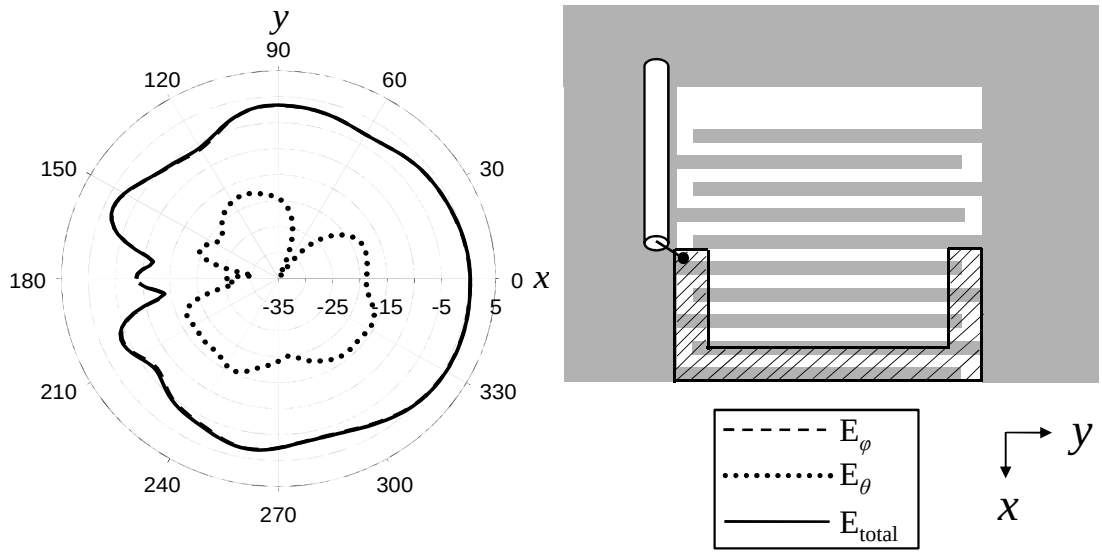

(a)

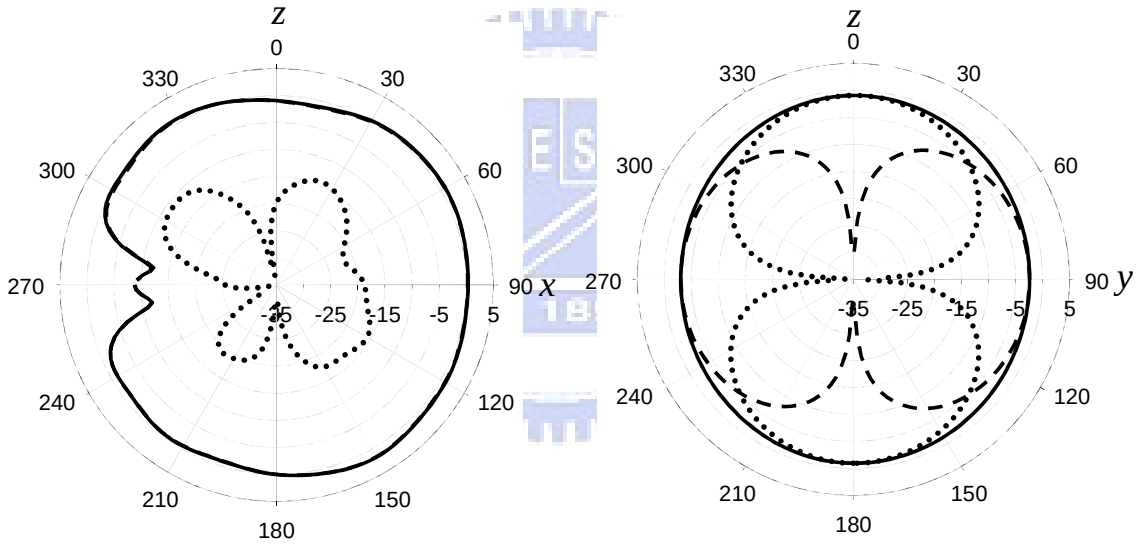

(b) (c)

Fig. 3.22. Measured 2-D radiation patterns for the proposed current driver with a lumped capacitor at 2.45 GHz. The driver is fabricated on the ground plane of 50 mm by 100 mm. (a) *xy* plane. (b) *xz* plane. (c) *yz* plane.

TABLE V
MEASURED GAINS AT 2.45 GHZ FOR THE CURRENT DRIVER WITH A PRINTED CAPACITOR

	xy plane	*xz* plane	*yz* plane
Peak gain (dBi)	0.70	1.73	0
Average gain (dBi)	-2.30	-0.22	-1.16

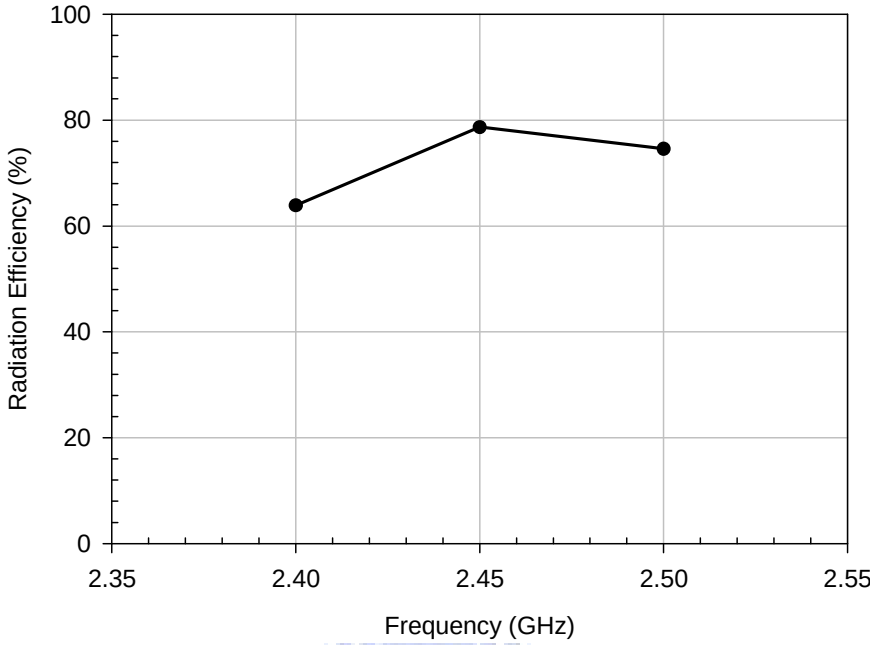

Fig. 3.23. Measured radiation efficiency for the current driver with a printed capacitor.

The measured 2-D radiation patterns in the three principal planes at 2.45 GHz are shown in Fig. 3.22. It is predictable that the patterns are similar to those shown before for the current driver designed with a lumped capacitor. As shown in the figure, the total-power radiation patterns E_{total} in the three principal planes are all nearly omin-directional. The corresponding values of measured peak and average gains in three principal planes are listed in TABLE V. In *xz* plane, the measured average gain is about 0 dBi, and the measured peak gains in three principal planes are all above 0 dBi. Fig. 3.23 gives the measured antenna radiation efficiency, where the efficiency varies from 64% to 79% over the band for 2.4 GHz WLAN application. It is worth noting that the measured efficiency comes to a good agreement with the simulated results. This is because that the ohmic loss caused by the printed capacitor is considered in the simulation. The current driver is demonstrated to have good radiation characteristics with the lumped capacitor replaced with a printed one. The photograph of the fabricated current driver with a printed capacitor is shown in Fig. 3.24.

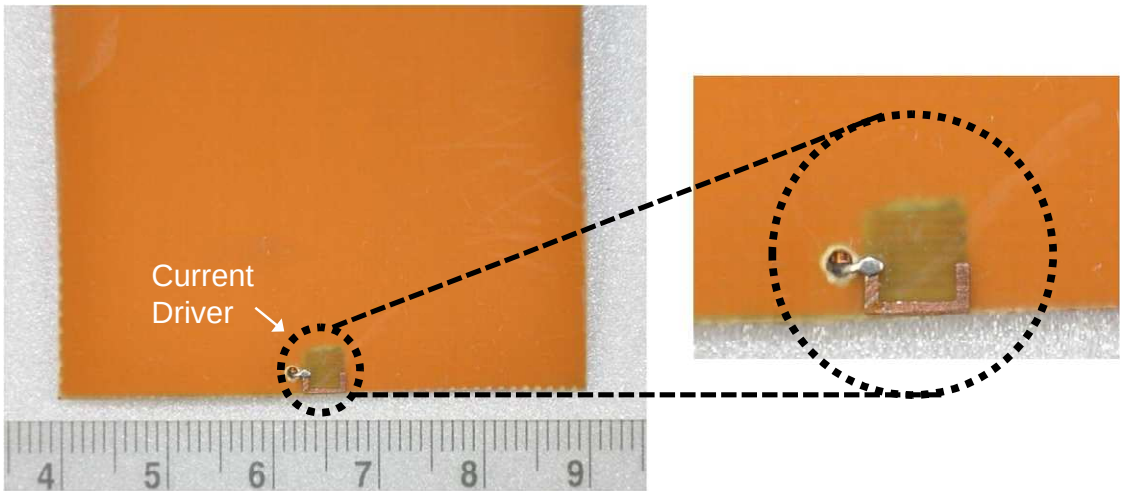

(a)

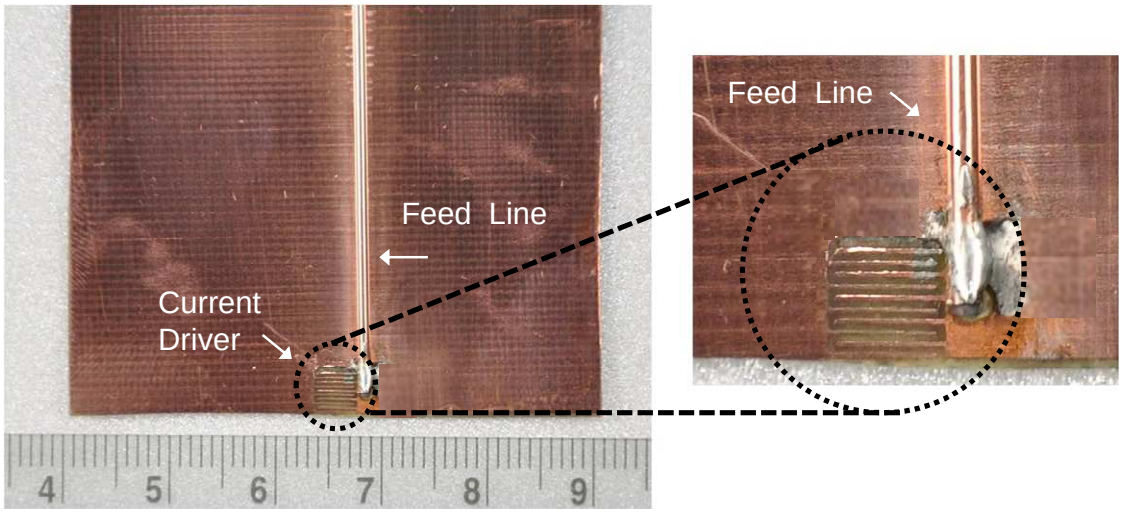

(b)

Fig. 3.24. Photograph of the fabrication for the proposed current driver with a printed capacitor. (a) Top view. (b) Bottom view.

Chapter 4 DESIGN OF THE DUAL-BAND CURRENT DRIVER

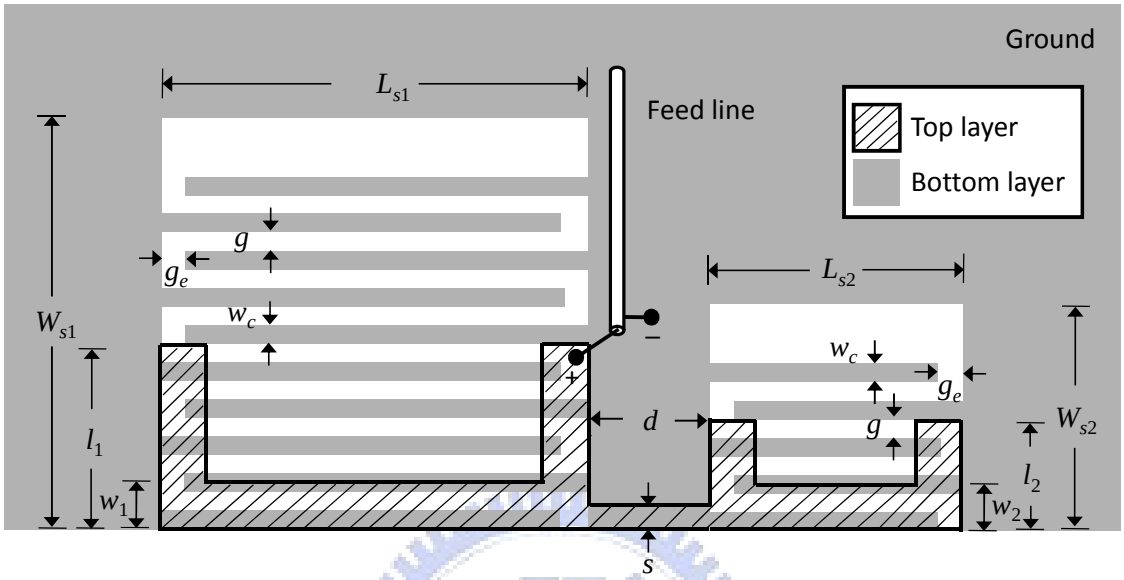

Fig. 4.1. Configuration of the dual-band current driver for WLAN 2.4/5.2 GHz applications.

TABLE VI
Detailed dimensions for the dual-band current driver

parameter	L_{s1}	Ws_1	N_1	l_1	w_1	d	$g = g_e$
unit(mm)	4	4	10	2	0.5	2	0.2
parameter	L_{s2}	Ws_2	N_2	l_2	w_2	s	w_c
unit(mm)	2.5	2.1	5	1.2	0.5	0.2	0.2

With the rapid development of wireless communications, the hand-held devices must be capable of multiband operation to tackle with different demands of wireless communication. However, as mentioned in Introduction, the overall size of the devices become smaller and smaller, and the space allocated for antenna design is very limited, especially for those in client terminal such as PCMCIA card or USB dongle. Thus, it is necessary to design a light weighted and low cost multiband antenna to integrate various applications. Given the compactness and design flexibilities, the current driver is a good candidate to meet the requirement. In this chapter, a dual-band current driver for WLAN 2.4/5.2 GHz applications is developed by combing two single-band current drivers. Both the simulation and measurement results are provided to evaluate the dual-band current driver.

4-1 GEOMETRY

To achieve WLAN 2.4/5.2 GHz applications, the developed dual-band current driver consists of two current drivers, one is designed for 2.4 GHz, and the other is for 5.2 GHz. They are fabricated on an FR4 substrate with thickness of 0.4 mm and dielectric constant $\varepsilon_r = 4.4$. The substrate size is the standard size for PCMCIA applications, which is $L \times W$ = 50 mm × 100 mm. The dual-band driver is fabricated on the center of the shorter ground edge *L*. To reduce cost and increase design flexibilities, the driver is designed by employing a printed interdigital capacitor as discussed in section 3.4. This makes the dual-band current driver easier to fabricate in the standard industrial process.

Fig. 4.1 shows the detailed configuration of the proposed dual-band current driver. The driver is printed on both sides of the substate. As mentioned above, the dual-band current driver is designed by combining two current drivers. As seen in the figure, the larger current driver in the left side is utilized for WLAN 2.4 GHz applications, and the smaller one in the right side is for WLAN 5.2 GHz applications. Each driver comprises a U-shaped metal strip on the top layer and the slot with a printed internal interdigital capacitor on the bottom layer. The two current drivers are connected with a thin metal strip on the top layer with width *s* and length *d*. The U-shaped strip is placed right above the slot with the strip edge aligned with the slot edge. The strip width and the arm length of the U-shaped metal strip are designated as *w* and *l*, respectively. The interdigital capacitor is defined by the parameter shown below, the figure width w_c, the gap between figures *g*, the gap at the end of the fingers g_e, and figure number N. The finger length varies with the slot length L_s. Also, the slot width W_s can be larger than the interdigital capacitor requires. Just ensure that the slot width must be large enough to accommodate N figures kept at the gap distance *g*. The current driver is fed by a 50 Ω transmission line, which can be a coaxial line or a microstrip line. The feed line is placed in between the current drivers with the positive terminal connected to one arm of the U-shaped metal strip for the 2.4 GHz current driver and the negative terminal connected to the ground plane near the slot edge of the 2.4 GHz current driver. The antenna occupies the size of only 8.5 mm × 4 mm, which is still very compact. The detailed dimension for the antenna is listed in TABLE VI. The design parameters for the 2.4 GHz and the 5.2 GHz current

driver are designated with suffix 1 and 2, respectively. Notice that the overall size for the 2.4 GHz current driver with printed interdigital capacitor is the same as given in section 3.4. This suggested that the properties of the 2.4 GHz current driver are not affected with the combination of the 5.2 GHz current driver for dual-band operation. As will shown later in the simulation, this property is important for the design of the dual-band current driver.

4-2 DUAL-BAND CURRENT DRIVER DESIGN

In this section, the detailed design procedures for the developed dual-band current driver are presented. Normally, for the miniaturized dual-band antennas, the antenna characteristics are generally affected by various parameters simultaneously through the complicated radiation mechanism. This makes the antenna difficult to design. However, it is not the case for the current-driver based dual-band antenna design. The dual-band current driver comprises two single-band current drivers, 2.4 GHz current driver and 5.2 GHz current driver. As will be demonstrated later, the interaction between two drivers is very minor over the band for 2.4 GHz WLAN applications. In other words, the performance of the 2.4 GHz current driver is basically unaffected by the combination with the 5.2 GHz current driver. Based on the fact stated above, the design procedures for the dual-band current driver are easy and straightforward. This section is divided into five parts. 4-2-1 will discuss the interaction between two current drivers, which gives the valuable results that the overall performance at 2.4 GHz is almost not influenced by the 5.2 GHz current driver. Thus, the two desired bands can be designed separately. The lower band operation is achieved by the parameter study of the 2.4 GHz current driver, which given in 4-2-2. After finishing the design of the 2.4 GHz current driver, the higher band performance is only affected by the 5.2 GHz current driver and the metal strip connected with two current drivers. Section 4-2-3 presents the parameter study of the 5.2 GHz current driver. The effect of the thin metal strip connected with two current drivers is investigated in 4-2-4. Finally, the ground size effect is discussed in 4-2-5. All the simulation results in this section are obtained using Ansoft High Frequency Structure Simulator (HFSS) [28]. The FR4 substrate loss is considered in the simulation with the loss tangent of 0.02. In the following, the parameters in the simulation are the same as

given in TABLE VI without specification.

4-2-1 Interaction between two current drivers

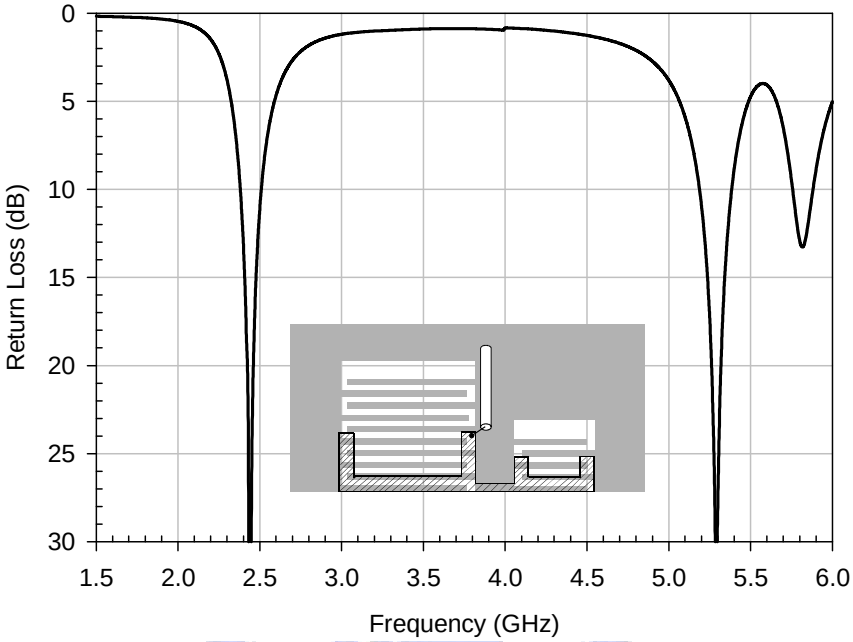

(a)

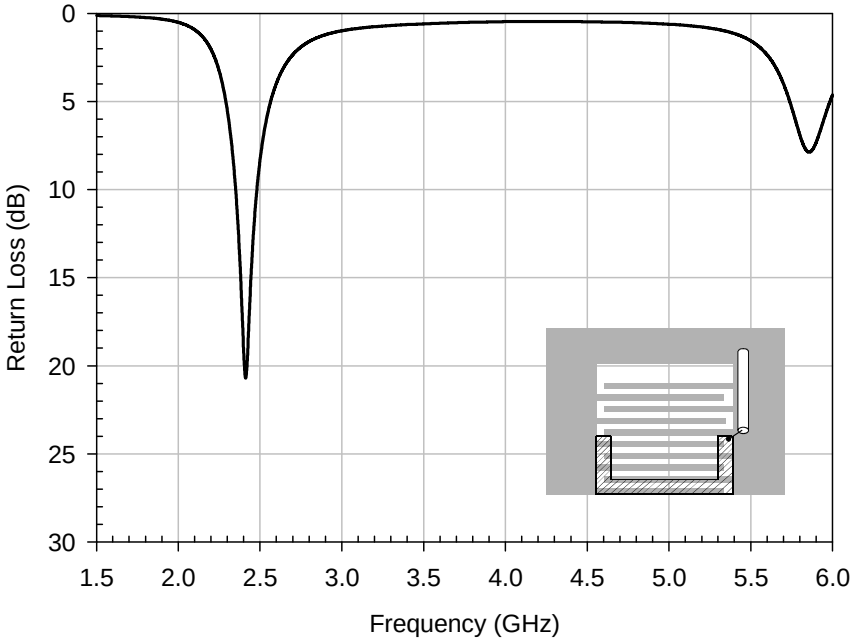

(b)

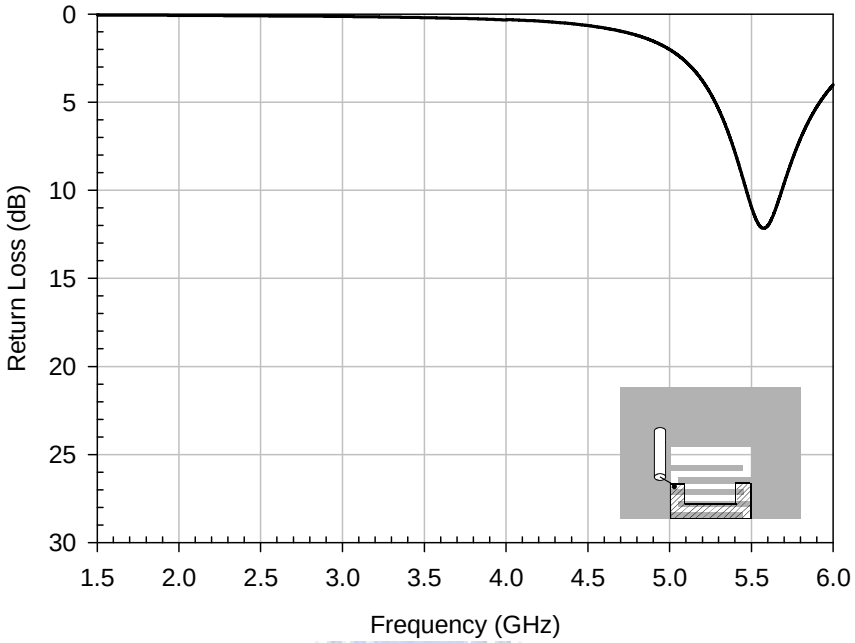

(c)

Fig. 4.2. Simulated return loss for the current driver with three configurations. The structure parameters are the same as listed in TABLE VI without particular specification. (a) Two current drivers for WLAN 2.4/5.2 GHz applications. (b) Single current driver for WLAN 2.4 GHz applications. (c) Single current driver for WLAN 5.2 GHz applications.

In this section, we are going to discuss the interaction between two current drivers, which is combined together for 2.4/5.2 GHz dual-band operation. The simulated return loss for the three configurations of current driver are considered including (a) two current drivers for WLAN 2.4/5.2 GHz dual-band operation, (b) the standalone current driver for WLAN 2.4 GHz, and (c) the standalone current driver for WLAN 5.2 GHz, as shown in Fig. 4.2. As seen in Fig. 4.2(a), the dual-band operation for WLAN 2.4/5.2 GHz is easily achieved by combining two current drivers. Fig. 4.2(b) shows that the resonance in the higher band at the center frequency of about 5.8 GHz is produced by the 2.4 GHz current driver. This has been mentioned in section 3-4 that the interdigital capacitor will introduce the additional non-radiative resonance, which can be avoided by replacing the printed capacitor to the lumped one. Compare Fig. 4.2(a) and (b). The performance at 2.4 GHz is almost unchanged with the combination of the 5.2 GHz current driver. This means that the 2.4 GHz current driver can be designed independently. The performance of the stand-alone 5.2 GHz current driver is depicted in Fig. 4.2(c), where the center frequency is at about 5.6 GHz with poor impedance matching. This suggests the

combination with the 2.4 GHz current driver affects both the improve impedance matching and center frequency in the higher band.

The reason that the combination with 5.2 GHz current driver has no obvious effect on the performance at 2.4 GHz is very straightforward. As has been shown before, the operation of the current driver relies on the capacitive coupling between the top layer and bottom layer. However, the capacitance between the two layers of the 5.2 GHz current driver is very small for the 2.4 GHz signal. The input impedance looking into the 5.2 GHz current driver is nearly open so the performance at 2.4 GHz depends only on the 2.4 GHz current driver. When it comes to 5.2 GHz operation, it is totally different. The 5.2 GHz signal can easily pass from the top layer to the bottom layer of the 2.4 GHz current driver. Moreover, the feed line is not directly connected to the 5.2 GHz current driver, which is connected through the thin metal strip on the top layer with a length *d* determined by the distance between the two current drivers. The length *d* lengthens the path of the ground plane for the 5.2 GHz current driver, so it has the effect on the center frequency, which will be demonstrated later in the parameter study of the thin metal strip. Thus, the higher band operation is determined not only by the 5.2 GHz current driver but also by the 2.4 GHz current driver and the thin metal strip connected with two drivers.

Based on the discussion above, the design procedures for the dual-band current driver are given as follows. The structure parameters for 2.4 GHz current driver has to be determined at first to ensure the proper operation in 2.4 GHz since the antenna performance at 2.4 GHz band is only affected by 2.4 GHz current driver. Then, by properly designing the 5.2 GHz current driver and the thin metal strip connected to the two current drivers, the higher band performance at 5.2 GHz can be achieved.

4-2-2 Parameter study of the 2.4 GHz current driver

As stated before, the frequency response in WLAN 2.4 GHz is not influenced by the combination with 5.2 GHz current driver. However, the antenna performance in WLAN 5.2 GHz is affected by both 2.4 and 5.2 GHz current drivers. Thus, to simplify the design procedure, the structure parameters for 2.4 GHz must be determined at first to ensure the proper operation in the lower band. In this section, the effects of the 2.4 GHz current driver will be presented through the parameters study on the return loss.

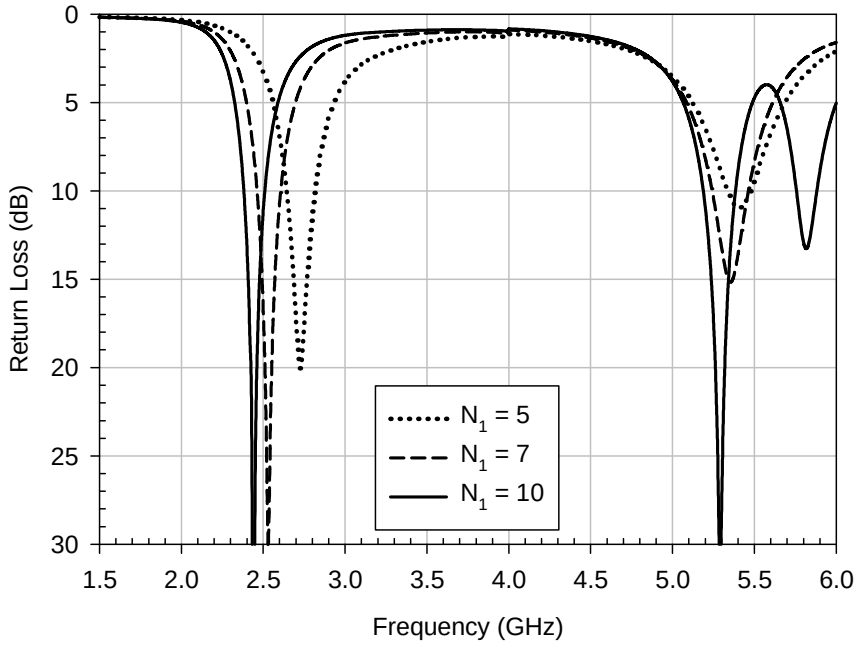

Fig. 4.3. Simulated return loss for various finger number N_1 of the interdigital capacitor of the 2.4 GHz current driver.

Fig. 4.3 shows the simulated return loss for various finger number N_1 of the interdigital capacitor. As has been discussed before, the capacitor in the current driver is critical to determine the center frequency. The center frequency moves lower with the higher capacitance. This is also observed for the current driver with printed interdigital capacitor. As shown in the figure, the center frequency moves lower with the higher finger number. Furthermore, it is observed that the frequency shift moves slower when N_1 varies from 10 to 7 (90 MHz from 2.44 GHz to 2.53 GHz), as compared to the frequency shift when N_1 varies from 7 to 5 (290 MHz from 2.44 GHz to 2.73 GHz). This is because of that the finger is removed from top to bottom in the slot. However, the bottom finger is more important than the top one because it receives more capacitive coupling from the top U-shaped metal strip. It is also noticed that the finger number N_1 has some effects on the impedance matching and center frequency in 5.2 GHz, which confirms the results obtained previously

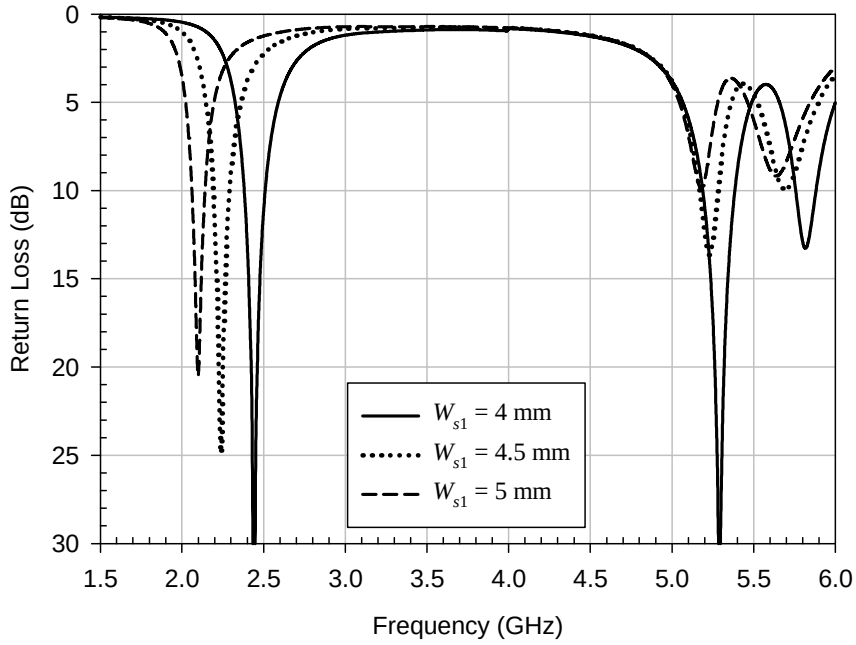

Fig. 4.4. Simulated return loss for various slot width W_{s1} of the 2.4 GHz current driver.

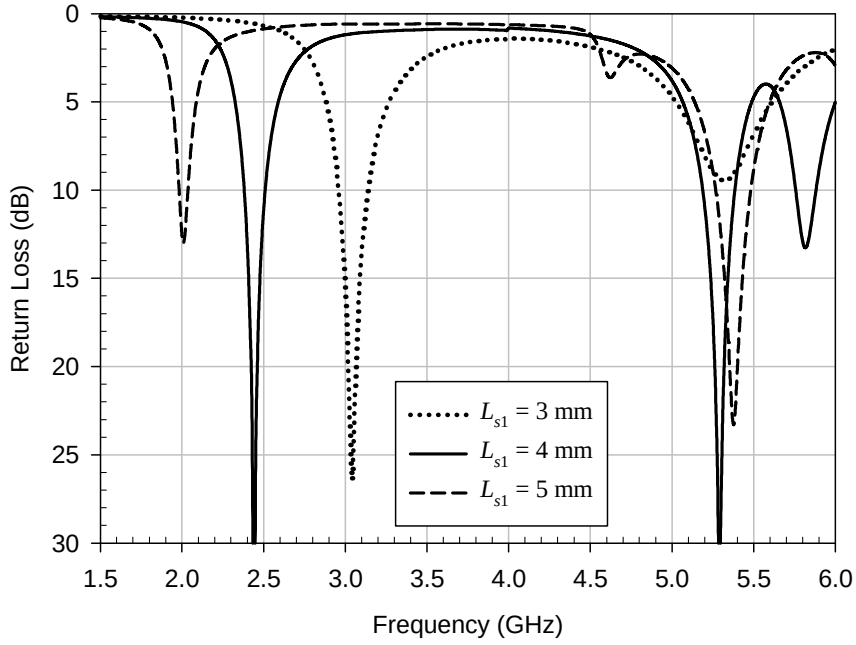

Fig. 4.5. Simulated return loss for various slot length L_{s1} of the 2.4 GHz current driver.

Similarly, the slot width W_{s1} for the current driver exhibits the same capability as the capacitor does that can change the center frequency without affecting the impedance matching. The simulated return loss shown in Fig. 4.4 helps to demonstrate this property. It shows that the center frequency moves from 2.44 GHz to 2.09 GHz as the slot width

W_s changes from 4 mm to 5 mm while maintaining the good impedance matching. As expected, the slot width also has effect on the antenna performance in the higher band. Moreover, it is demonstrated before that the current driver with larger slot width and smaller capacitance has a wider bandwidth. Although not shown here, this property still holds for the dual-band current driver. In this thesis, the slot width and finger number are chosen to be 4 mm and 10, which is adequate for WLAN 2.4 GHz operation.

The effect of the slot length is examined in the following. The function of the slot length L_{s1} can also control the center frequency as discussed in Section III, where the center frequency moves lower with increasing slot length. This can be verified in Fig. 4.5, where the simulated return loss with various slot length is demonstrated. As shown in the figure, the frequency shifted about 1 GHz is observed with slot width L_{s1} varying from 3 mm to 5 mm. Since the finger length varies with the slot length L_{s1}, the frequency shift range caused by the slot length is larger than others parameters do. Normally, the slot length is chosen as equal to the slot width to make the current driver occupied in a small square. In this case, the slot width and slot length are chosen to be 4 mm. Still, the frequency response at 5.2 GHz is influenced by the structure variation of the 2.4 GHz current driver.

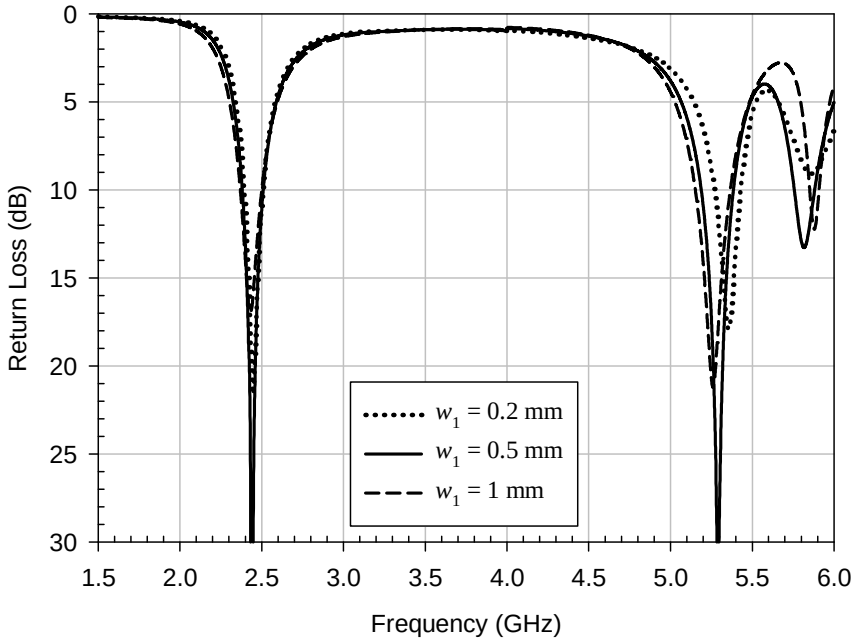

Fig. 4.6. Simulated return loss for various strip width w_1 of the 2.4 GHz current driver.

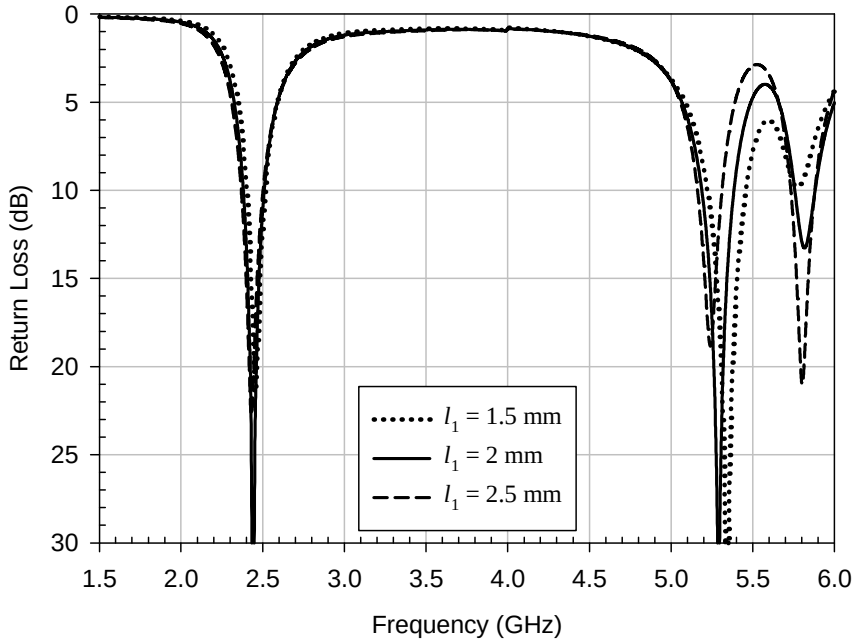

Fig. 4.7. Simulated return loss for various arm length l_1 of the 2.4 GHz current driver.

The effect of the strip width of the U-shaped metal strip on the top layer is investigated in Fig. 4.6. As discussed before, the strip width w_1 determines the amount of capacitive coupling from top layer to the bottom layer of the current drive, which controls the impedance matching but has little effect on the center frequency. Thus, the dual-band current driver can be well matched in the lower band with appropriate value w_1. For the dual-band current driver, the slot width is chosen to be 0.5 mm to achieve the best impedance matching with the bandwidth of 130 MHz from 2.38 GHz to 2.51 GHz, and the return loss at 2.44 GHz is near 40 dB. It is also observed that the strip width w_1 has the effect on the return loss in the higher band.

In Fig. 4.7, the simulated return loss for various arm length l_1 of the U-shaped metal strip is demonstrated. There are some variations of the impedance matching observed in the figure with the center frequency nearly fixed. This is similar to the effect of the strip width on the return loss. It shows that the impedance matching is depending on the coupling strength. As seen in the figure, the arm length l_1 is determined to be 2 mm to obtain adequate coupling strength for the good impedance matching.

4-2-3 Parameter study of the 5.2 GHz current driver

After finishing the design of the 2.4 GHz current driver, the lower band performance at 2.4 GHz for the dual-band current driver is achieved. In the following, the antenna performance in the higher band at 5.2 GHz will be designed through the parameter study of the 5.2 GHz current driver.

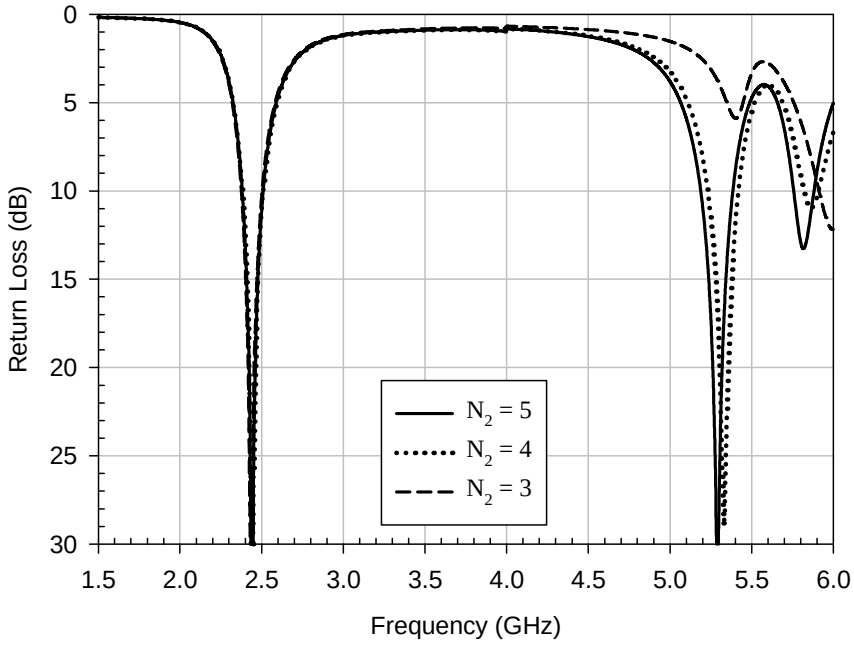

Fig. 4.8. Simulated return loss for various finger number N_2 of the 5.2 GHz current driver.

Fig. 4.8 shows the simulated return loss for different finger numbers N_2. As seen in the figure, the center frequency is shifted higher with a frequency shift of about 40 MHz when N_2 varies from 5 to 4. However, the impedance matching is deteriorated when N_2 changes from 4 to 3. This is due to the fact that the finger number not only determines the capacitance but also has an effect on the coupling strength between the top layer and the bottom layer of the current driver, which can control the impedance matching. Unlike the property that the 2.4 GHz current driver demonstrated before, the 5.2 GHz current driver is more sensitive to the variation of the coupling strength. This leads to the abrupt impedance deterioration when N_2 is set to be 3. In this case, the figure number must be larger than 3 to achieve the adequate coupling strength. Moreover, as expected, the performance in the lower band is unrelated to the 5.2 GHz current driver.

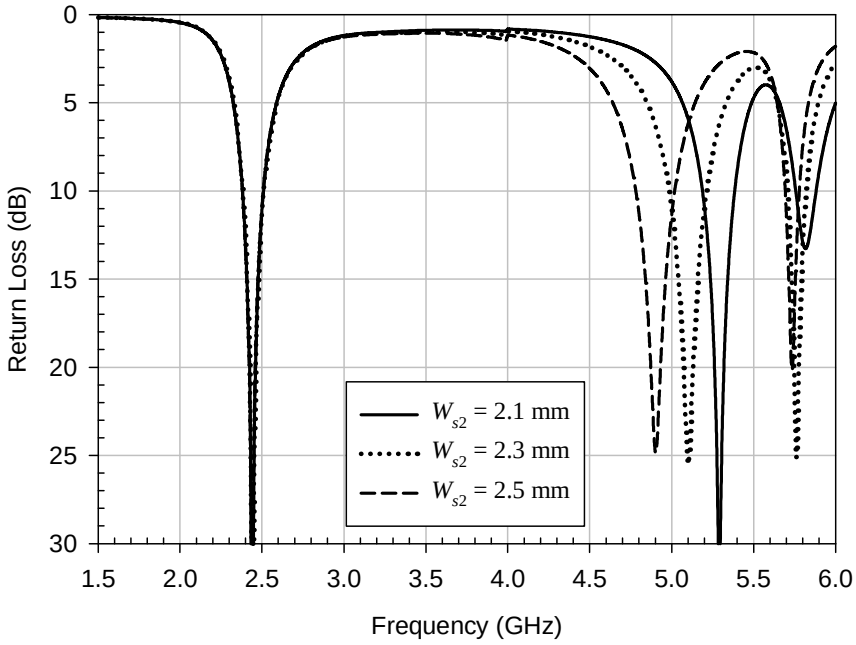

Fig. 4.9. Simulated return loss for various slot width W_{s2} of the 5.2 GHz current driver.

The simulated return loss for the 5.2 GHz current driver with various slot width W_{s2} is given in Fig. 4.9. As shown in the figure, about 400 MHz frequency shift in the higher band is observed. The center frequency moves lower from 5.29 GHz to 4.9 GHz when the slot width increases from 2.1 mm to 2.5 mm. Since the variation of the slot width has no obvious effect on the coupling strength between the top layer and bottom layer, good impedance matching maintains despite the frequency shift caused by the slot width. Also, the performance in the lower band is not changed with the variation of W_{s2}.

As mentioned earlier, the slot length of the current driver can affect the center frequency. Fig. 4.10 is used to demonstrate this property, where the simulated return loss is shown as a function of slot width L_{s2}. The center frequency moves higher from 4.72 GHz to 5.29 GHz when the slot width decreases from 3 mm to 2.5 mm. However, it is observed that the impedance matching becomes worse when the slot width is lowered to 2.3 mm. Similarly, this is related to the coupling reduction as already mentioned since the figure length of the printed capacitor varies with the slot length. Therefore, the slot length cannot be designed too small. Otherwise, the required coupling strength is hard to achieve. This will caused serious impedance deterioration. Moreover, to design the dual-band current driver with a compact size, the slot width and length is chosen as close as

possible, which are 2.5 mm and 2.1 mm respectively with consideration about the impedance matching and size reduction.

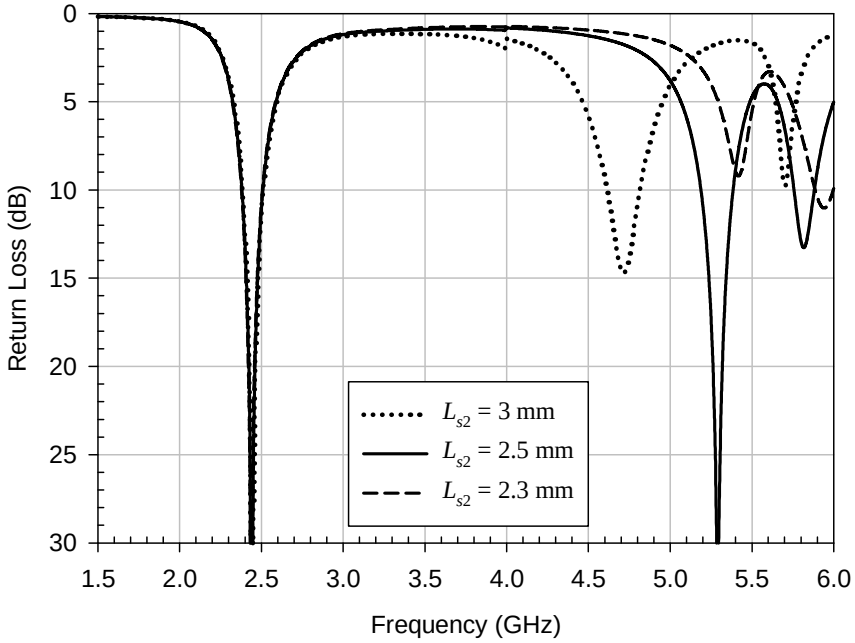

Fig. 4.10. Simulated return loss for various slot length L_{s2} of the 5.2 GHz current driver.

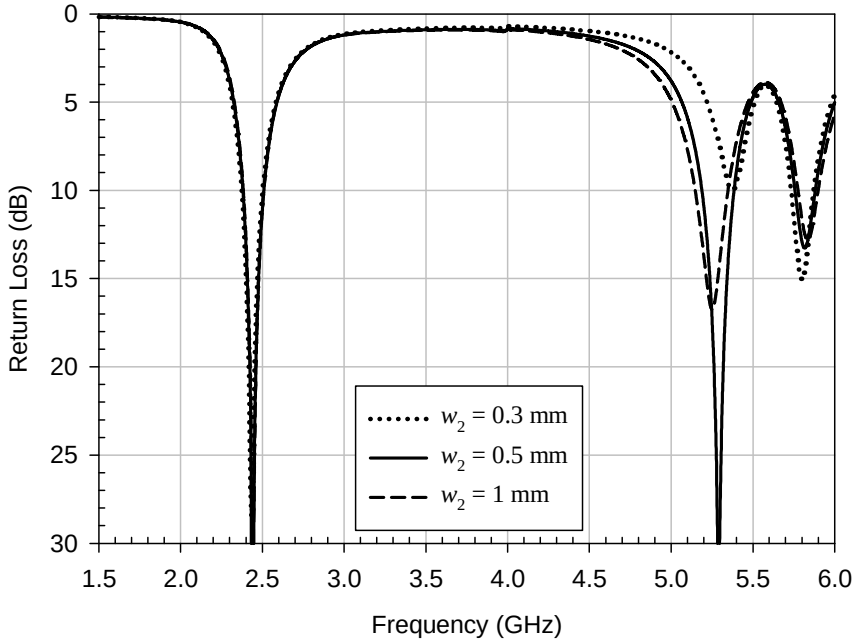

Fig. 4.11. Simulated return loss for various strip width w_2 of the 5.2 GHz current driver.

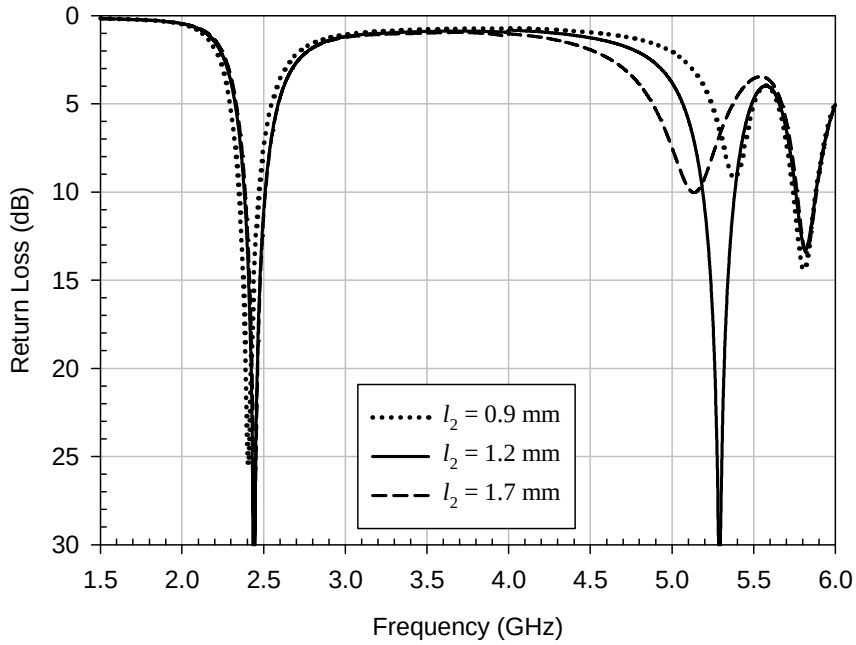

Fig. 4.12. Simulated return loss for various arm length l_2 of the 5.2 GHz current driver.

The effect of strip width relating to the coupling strength in the structure of the current driver is investigated,. The good impedance matching is obtained by properly designing the coupling strength. Fig. 4.11 presents the simulation results of return loss for different strip width w_2 of the 5.2 GHz current driver. As expected, the strip width has the effect on the impedance matching. As shown in the figure, the impedance matching varies slowly with the decreasing strip width w_2 from 1 mm to 0.5 mm, but it deteriorates rapidly when the slot width decreased to 0.3 mm. The strip width is chosen to be 0.5 mm, which shows the best impedance matching. Also, the strip width w_2 has little effect on the performance at 2.4 GHz.

In addition to the strip width w_2, the arm length l_2 also affects the coupling strength of the top layer and the bottom layer for the 5.2 GHz current driver. The more is the arm length l_2, the stronger is the coupling strength. Fig. 4.12 shows the simulated return loss with arm length varies from 0.9 mm to 1.7 mm. The impedance matching varies rapidly with various arm length. To achieve good impedance matching, the coupling arm length must be carefully designed for adequate coupling strength, which is 1.2 mm in this case.

From all the discussion shown above, it indicates that the 5.2 GHz current driver can be easily designed to meet the higher band operation of the dual-band current driver. Basically, the property of the 5.2 GHz current driver is similar to the one of the 2.4 GHz current driver except that it is more sensitive to the coupling strength between the top layer and bottom layer. As long as the required coupling for the 5.2 GHz is met, the center frequency can be tuned by the slot width W_{s2}, slot length L_{s2}, and figure number N_2 with little effect on the impedance matching.

4-2-4 Effects of the thin metal strip connected with two current drivers

In addition to the 5.2 GHz current driver, the thin metal strip used to connect two current drivers also has effects on the antenna performance in the higher band. In this section, the effect of the thin metal strip is considered through the parameter study as the function of the strip length *d* and strip width *s*.

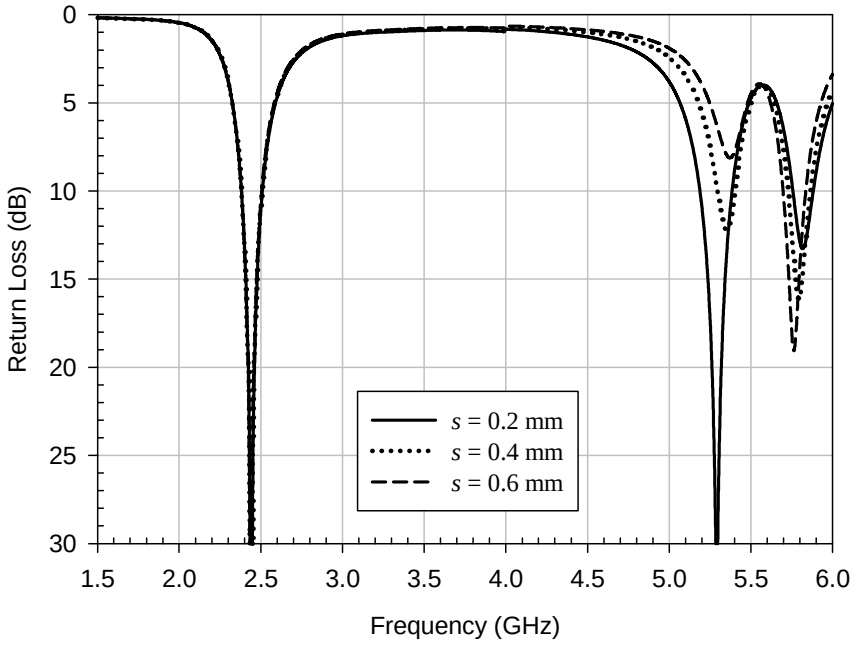

Fig. 4.13. Simulated return loss for various strip width *s* of the thin metal strip used to connect two current drivers. The other parameters are the same as given in TABLE VI.

At first, Fig. 4-13 shows the simulated return loss for various strip width *s*. It is seen that the strip width *s* plays a pivotal role in determining the impedance matching. As

observed in the figure, the impedance matching becomes worse as strip width *s* increases from 0.2 mm to 0.6 mm, and the center frequency is almost unchanged.

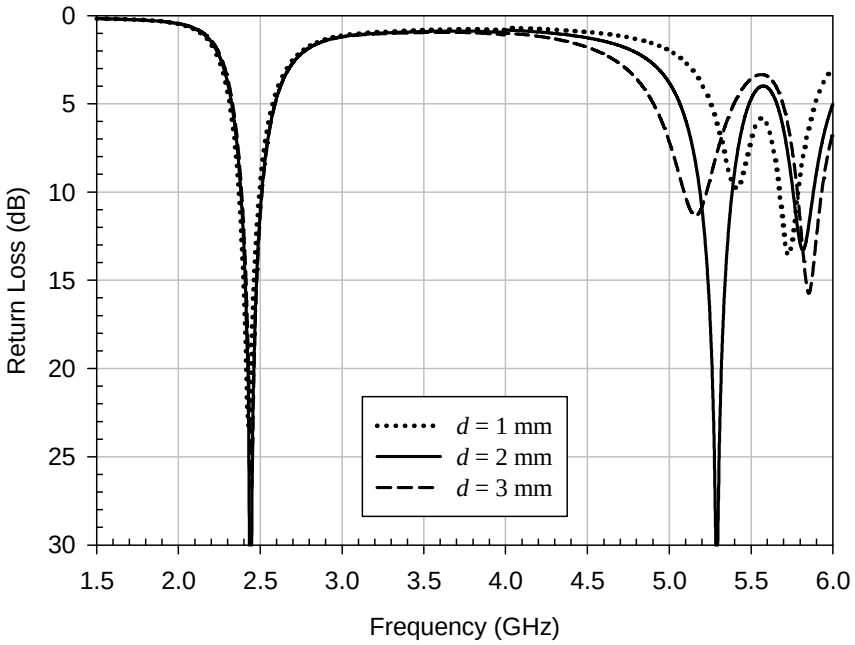

Fig. 4.14. Simulated return loss for various strip width *s* of the thin metal strip used to connect two current drivers. The other parameters are the same as given in TABLE VI.

Secondly, the effect on the return loss caused by strip length *d* is clearly demonstrated in Fig. 4-14. It shows that both center frequency and impedance matching in the higher band are affected by the strip length *d* of the thin metal strip. The center frequency moves from 5.43 GHz to 5.13 GHz when strip length *d* varies from 1 mm to 3 mm. For the dual-band current driver, the distance *d* is chosen to be 2 mm to accommodate the feed line placed in between the drivers while keeping the whole size compact.

According to the discussion in section 4-2-3 and 4-2-4, the performance in the higher band for the dual-band current driver is easily achieved with a compact size through the proper design of the 5.2 GHz current driver and the thin metal strip connected with two current drivers. Moreover, it is demonstrated in the simulation that the return loss in the lower band is almost unaffected with the combination with the 5.2 GHz current driver. This property greatly reduces the design complexity that makes the two bands of the dual-band current driver can be designed separately.

4-2-5 Ground size effect

After discussing all the structure parameters of the current drivers, the ground size effect on the performance of the proposed dual-band antenna based on the current driver is investigated in this section. Fig. 4.15 illustrates the simulated return loss for the current drivers with different ground planes of 40×50 mm_2, 50×100 mm_2, and 170×250 mm_2. As seen in the figure, the three curves are nearly overlapped with each other. It suggests that the antenna performance is almost not influenced by the ground size. This agrees with the previous results for the single 2.4 GHz current driver. Thus, the developed dual-band current driver is also suitable for various commercial applications due to its design flexibilities.

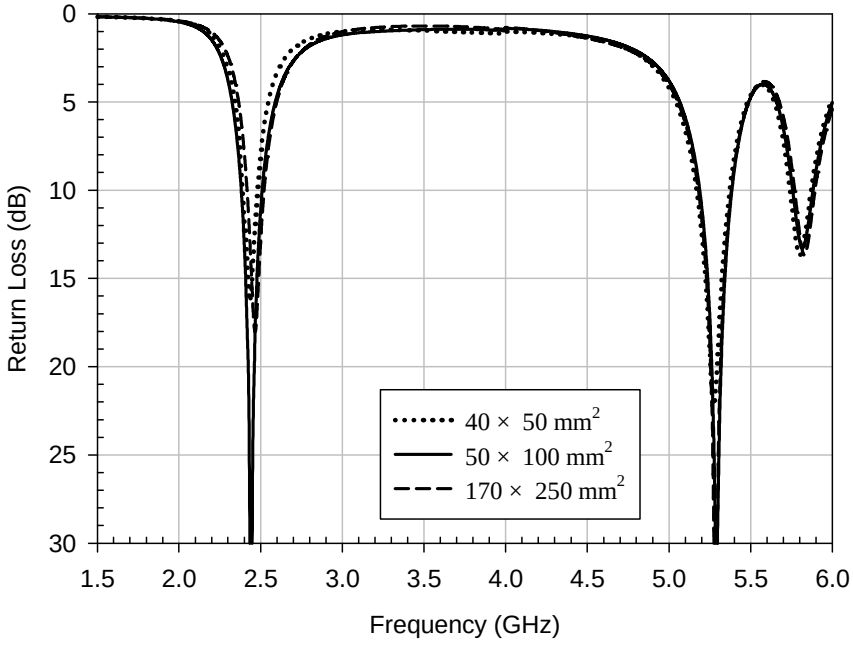

Fig. 4.15. Simulated return loss for the dual-band current driver fabricated on different substrate sizes. The other parameters of the dual-band current driver are the same as given in TABLE VI.

4-3 MEASUREMENT RESULTS

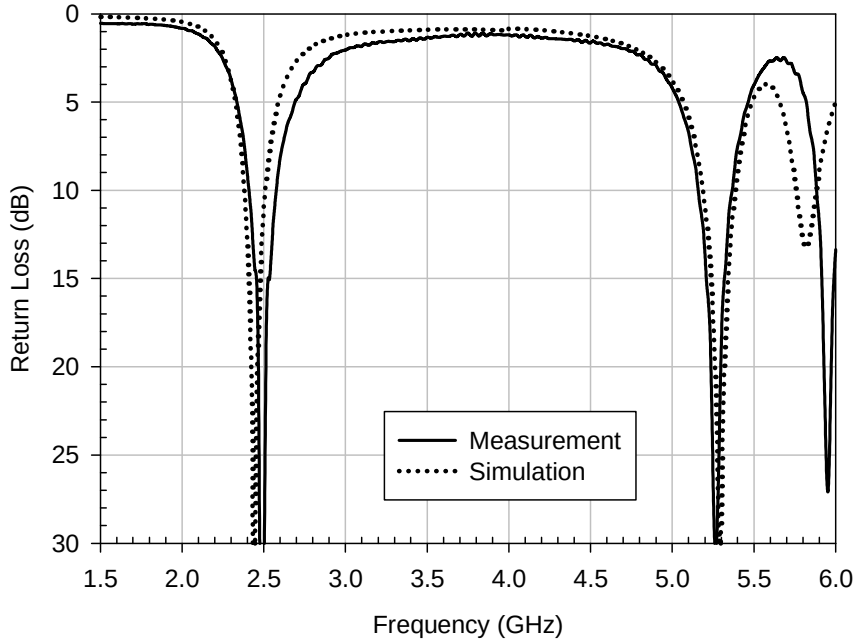

Fig. 4.16. Simulated and measured return loss for the dual-band current driver with a ground plane of 50 mm × 100 mm. The other parameters are the same as given in TABLE VI.

In this section, the measurement results and the related discussion are presented. Simulation and measurement results are compared in Fig. 4.16, which shows the simulated and measured return loss for dual-band current driver with a ground plane of size $L \times W$ = 50 mm × 100 mm. As seen in the figure, the simulated result basically agrees with the measured one. The measured center frequency in the low band is at 2.48 GHz with a 10-dB return-loss bandwidth of about 140 MHz, which covers the required band for IEEE 2.4 GHz WLAN operation. In the high band, the measured 10-dB bandwidth at the center frequency of 5.25 GHz satisfies the requirement for 5.2 GHz WLAN operation from 5.15 GHz to 5.35 GHz.

The measured 2D radiation patterns at 2.45 GHz in the three principal planes are illustrated in Fig. 4.17. The dual-band current driver comprising two current drivers lies in the *xy* plane. There are generally no nulls for the total-power radiation pattern E_{total} observed in the three principal planes, which is attractive to many applications. Also, it is noted that the measured patterns basically have the same shapes as the ones in the configuration of the single 2.4 GHz current driver shown before. This suggests that the

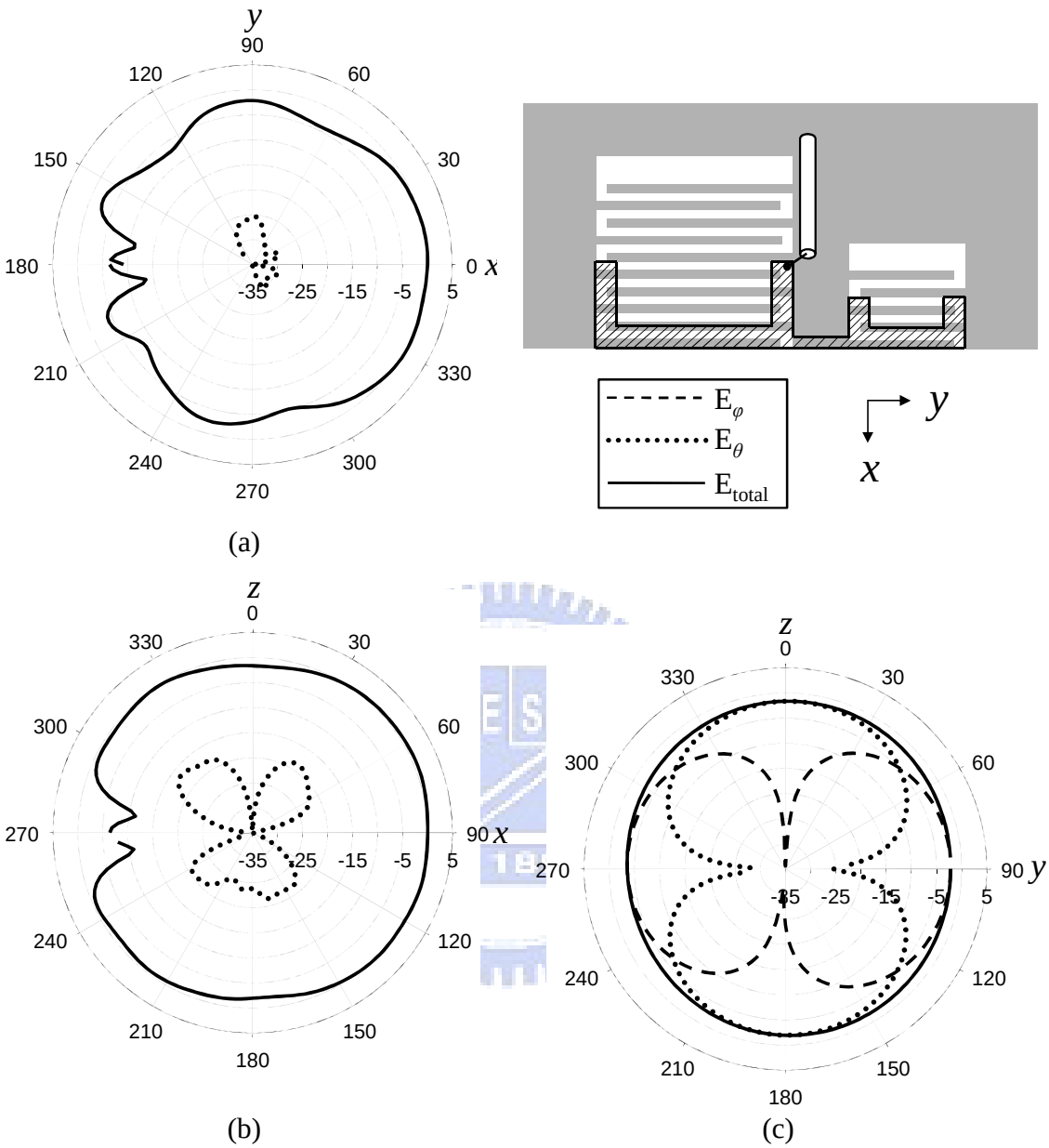

Fig. 4.17. Measured 2-D radiation patterns for the dual-band current driver at 2.45 GHz with a connected ground of 50 mm by 100 mm. (a) *xy* plane. (b) *xz* plane. (c) *yz* plane.

TABLE VII
MEASURED GAINS AT 2.45 GHZ FOR THE DUAL-BAND CURRENT DRIVER

2.45 GHz	*xy* plane	*xz* plane	*yz* plane
Peak gain (dBi)	0.50	0.65	-1.56
Average gain (dBi)	-2.85	-0.40	-2.32

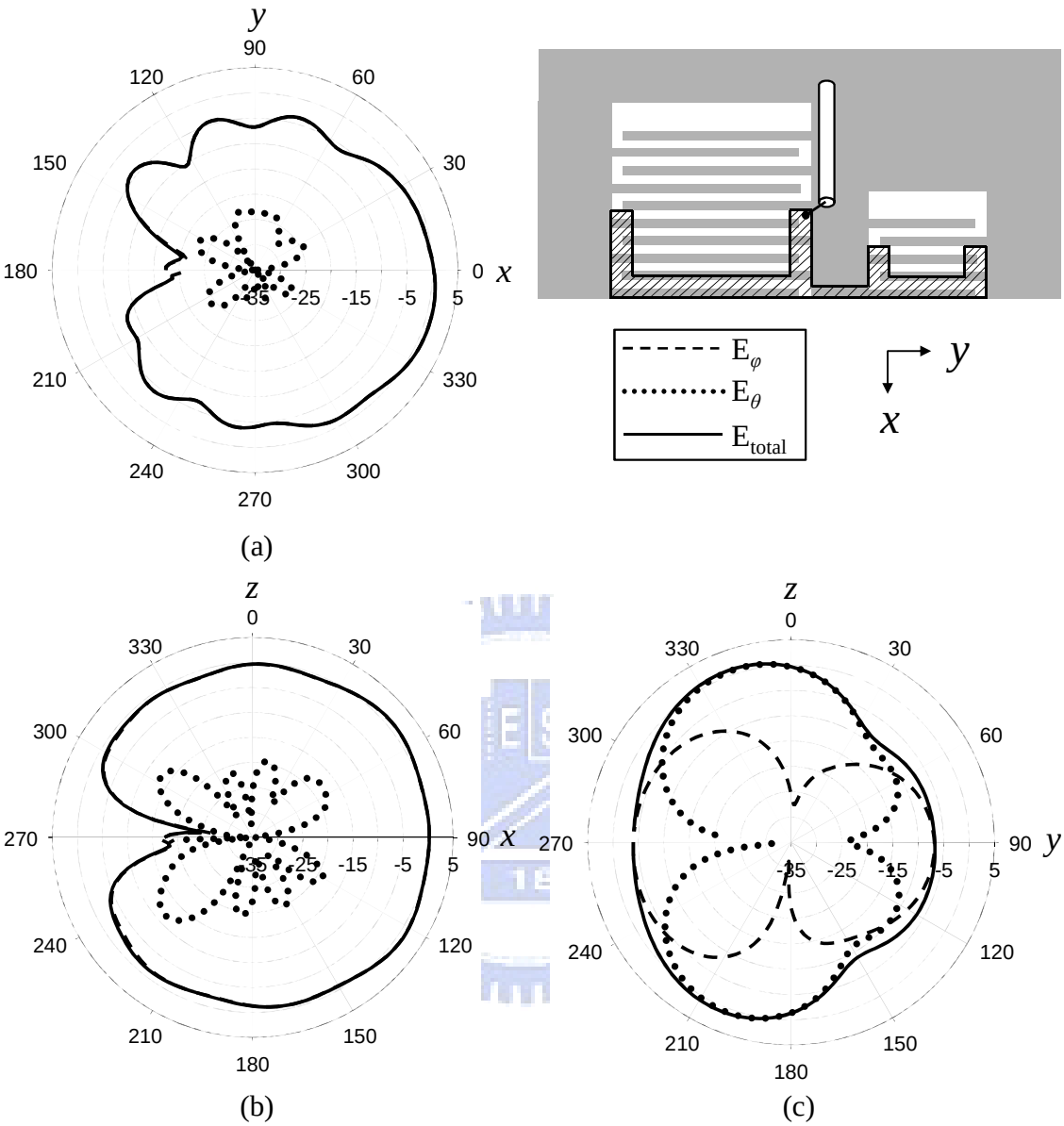

Fig. 4.18. Measured 2-D radiation patterns for the dual-band current driver at 5.2 GHz with a connected ground of 50 mm by 100 mm. (a) *xy* plane. (b) *xz* plane. (c) *yz* plane.

TABLE VIII
MEASURED GAINS AT 5.2 GHZ FOR THE DUAL-BAND CURRENT DRIVER

5.2 GHz	*xy* plane	*xz* plane	*yz* plane
Peak gain (dBi)	0.98	1.10	1.03
Average gain (dBi)	-3.46	-1.01	-2.62

combination with the 5.2 GHz current driver will also not influence the radiation characteristics of the 2.4 GHz current driver. The corresponding values of the peak gains and average gains are given in TABLE VII. The measured average gain for the nearly omni-directional pattern in *xz* plane is about -0.4 dBi.

Fig. 4.18 shows the measured 2D radiation patterns in the three principal planes at 5.2 GHz. The shapes of the radiation patterns are similar to the ones shown in Fig. 4.16 at 2.45 GHz except in the *yz* plane. This is caused by the asymmetry position of the 5.2 GHz current driver on the ground edge. In this thesis, the dual-band current driver is placed in the center of the shorter ground edge. Thus, the 5.2 GHz current driver is shifted a distance from the center of the ground plane. This distance shift causes the asymmetry patterns at 5.2 GHz but has minor effect at 2.45 GHz. The corresponding values of the measured peak gains and average gains are given in TABLE VIII. The measured average gain for the nearly omini-directional patterns in *xz* plane is about -1 dBi. Additionally, the measured radiation efficiency for both bands is illustrated in Fig. 4.19. The efficiency in 2.4 GHz WLAN varies between 63 % and 70 %. Over the bandwidth for WLAN 5.2 GHz, value of the radiation efficiency is between 52 % and 60 %. The 10 % difference between the antenna efficiency comes from the high dielectric loss in the high band. Finally, the photograph of the fabricated dual-band current driver is shown in Fig. 4.20.

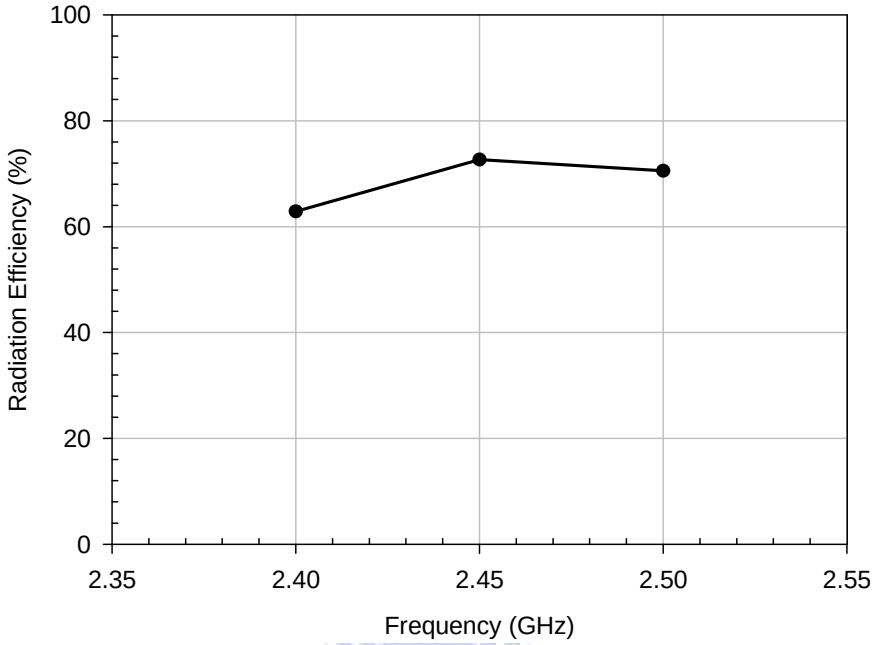

(a)

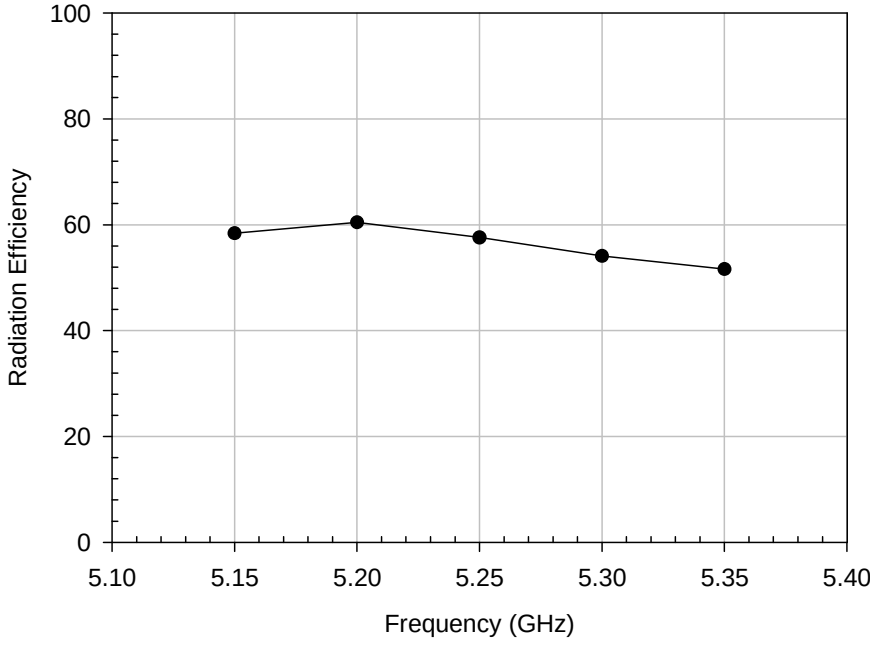

(b)

Fig. 4.19. Measured radiation efficiency for the dual-band current driver. (a) 2.4 GHz WLAN (b) 5.2 GHz WLAN

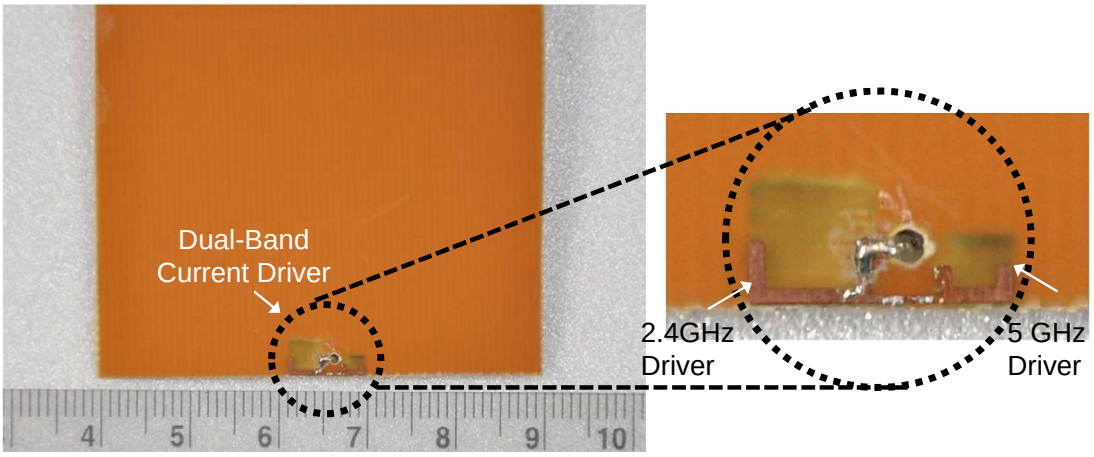

(a)

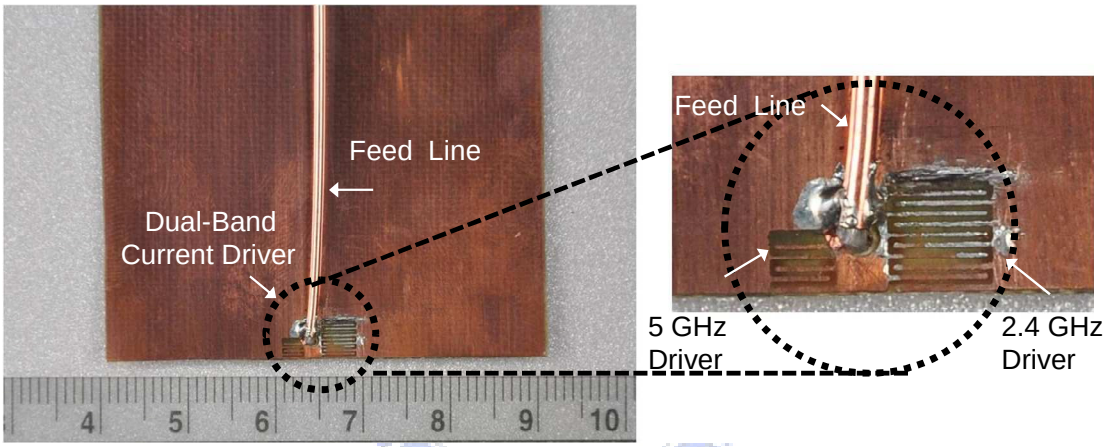

(b)

Fig. 4.20. Photograph of the fabrication for the proposed current driver with a printed capacitor. (a) Top view. (b) Bottom view.

Chapter 5 CONCLUSION

In this thesis, a new microwave component called current driver is proposed to activate the ground edge current for radiation. The main point of the current-driver based antenna is that the main radiator is the ground plane as opposed to the current driver. Therefore, the driver can be designed very small while good radiation properties are maintained. The equivalent circuit model of the current driver viewed as a miniaturized planar balun helps to explain the edge-current inducing mechanism. Also, the results of the parameter study for the current driver are consistent with the characteristics of the miniaturized balun. In addition, the current driver is shown to be insensitive to the ground size. This suggests that the current driver can be easily applied to various applications. The influence of the shielding box for the proximity circuitry near the current driver is also thoroughly investigated, which indicates that the effect of the shielding box on the performance of the current driver is minor even when the box is placed very close to the current driver.

Two antenna applications based on current driver is presented, one is for WLAN 2.4 GHz applications and the other is for WLAN 2.4/5.2 dual-band applications. For WLAN 2.4 GHz applications, the current driver can be implemented by a lumped capacitor or printed capacitor with the size of about 4 mm × 4 mm, which is only about 0.03 λ_0 × 0.03 λ_0 (λ_0 is the free-space wavelength at 2.45 GHz). The good radiation properties are achieved at 2.45 GHz with the measured radiation efficiency of above 60 % and the nearly omni-directional radiation patterns with the average gain of about 0 dBi. For WLAN 2.4/5/2 GHz applications, two drivers are combined together to achieve dual-band operation. The overall size is about 8.5 mm × 4 mm, which is still compact as compared to others miniaturized dual-band antenna. Basically, the radiation performance for the combined current drivers at 2.4 GHz is the same as the performance for the single 2.4 GHz current driver, which has the radiation efficiency over 60%. At 5.2 GHz, the measured radiation efficiency for the combined current drivers varies between 50% and 60 %, which is lower than the efficiency obtained at 2.45 GHz due to the highly lossy FR4 substrate in the high band. The nearly omni-directional patterns are observed at both 2.4 and 5.2 GHz. The current driver has advantages of compact size and ease of fabrication, so it is suitable for commercial applications.

REFERENCES

[1] H. Mosallaei and K. Sarabandi, "Magneto-dielectrics in electromagnetic: Concept and applications," *IEEE Trans. Antennas Propagat.*, vol. 52, no. 6, pp. 1558-1567, Jun. 2004.

[2] K. Buell, H. Mosallaei, and K. Sarabandi, "A substrate for small patch antennas providing tunable in miniaturization factors," *IEEE Trans. Microw. Theory Tech.*, vol. 54 pp. 135-146, Jan. 2006.

[3] H. Mosallaei and K. Sarabandi, "Design and modeling of patch antenna printed on magneto-dielectric embedded-circuit metasubstrate," *IEEE Trans. Antennas Propag.*, vol. 55, pp. 45-52, Jan. 2007.

[4] A. Erentok and R. W. Ziolkowski, "Metamaterial-inspired efficient electrically small antennas," *IEEE Trans. Antennas Propag.*, pp. 691-707, Mar. 2008

[5] P. Jin and R. W. Ziolkowski, "Low-Q, Electrically Small, Efficient Near-Field Resonant Parasitic Antennas," *IEEE Trans. Antennas Propag.*, pp. 2548-2563, Sep. 2009

[6] Y.-S. Wang, M.-C. Lee, and S.-J. Chung, "Two PIFA-related miniaturized dual-band antennas, " *IEEE Trans. Antennas Propagat.*, vol. 55, no.3, pp. 805-811, Mar. 2007.

[7] C.-J. Lee, K. M. K. H. Leong, and T. Itoh, "Composite right/left-handed transmission line based compact resonant antennas for RF module integration," *IEEE Trans. Antennas Propagat.*, vol. 54, no. 8, pp. 2283-2291, Aug. 2006.

[8] J.-G. Leee and J.-H. Lee, "Zeroth order resonance loop antenna," *IEEE Trans. Antennas Propag.*, vol. 55, nol 3, pp. 994-997, Mar. 2007

[9] Y.-S. Wang, M.-F. Hsu, and S.-J. Chung, "A Compact Slot Antenna Utilizing a Right/Left-Handed Transmission Line Feed," *IEEE Trans. Antennas Propagat.*, vol. 56, no. 3, pp. 675-683, Mar. 2008.

[10] S. Pyo, S.-M. Han, J.-W. Baik, and Y.-S. Kim, "A Slot-Loaded Composite Right/Left-Handed Transmission Line for a Zeroth-Order Resonant Antenna With Improved Efficiency," *IEEE Trans. Microw. Theory Tech.*, vol. 57, no. 11, pp. 2775-2782, Nov. 2009.

[11] R. C. Hansen, “Fundamental limitations in antennas,” *Proc. IEEE*, vol. 69, pp. 170–182, Feb. 1981.

[12] R. F. Harrington, “Effect of antenna size on gain, bandwidth, and efficiency,” *J. Res. Nat. Bureau Stand.*, vol. 64D, pp. 1–12, Jan. 1960.

[13] J. S. McLean, “A re-examination of the fundamental limits on the radiation Q of electrically small antennas,” *IEEE Trans. Antennas Propag.*, vol. 44, no. 5, pp. 672–676, May 1996.

[14] P. Vainikainen, J. Ollikainen, O. Kivekäs, and I. Kelander, “Resonator-based analysis of the combination of mobile handset antenna and chassis,” *IEEE Trans. Antennas Propagat.*, vol. 50, no. pp. 1433-1444, Oct. 2002.

[15] R. Hossa, A. Byndas, and M. E. Bialkowski, “Improvement of compact terminal antenna performance by incorporating open-end slots in ground plane,” *Microw. Opt. Technol. Lett*., vol. 14, no. 6, pp. 283–285, Jun. 2004.

[16] P. Lindberg and E. Öjefors, “A bandwidth enhancement technique for mobile handset antennas using wavetraps,” *IEEE Trans. Antennas Propagat.*, vol. 54, no. 8, pp. 2226-2233, Aug. 2006.

[17] Y.-S. Wang, J.-C. Lu, and S.-J. Chung, “A Miniaturized Ground Edge Current Choke—Design, Measurement, and Applications,” *IEEE Trans. Antennas Propagat*,, vol. 57, no. 5, pp. 1360-1366, May 2009.

[18] J. Villanen, J. Ollikainen, O. Kivekäs, and P. Vainikainen, “Coupling element based mobile terminal antenna structures,” *IEEE Trans. Antennas Propagat.*, vol. 54, no. 7, pp. 2142-2153, Jul. 2006.

[19] L. Huang and P. Russer, “Electrically Tunable Antenna Design Procedure for Mobile Applications,” *IEEE Trans. Microw. Theory Tech.*, vol. 56, no. 12 Part 1, pp. 2789-2797, Dec. 2008.

[20] M. Cabedo-Fabres, E. Antonino-Daviu, A. Valero-Nogueira, and M. Ferrando-Bataller, “Wideband radiating ground plane with notches,” in *Proc. IEEE Ant. And Propag. Soc. Int. Symp. Dig.*, Washington, DC, USA, July 2005, pp. 560-563.

[21] P. Lindberg, E. Öjefors, and A. Rydberg, “Wideband slot antenna for low-profile hand-held terminal applications, “ in *Proc.* 36th *European Microw. Conf. 2006*, Manchester, UK, Sept. 2006, pp. 1698-1701.

[22] C.-L. Li, J.-P. Chang, and L.-J. Wong, “Miniature planar notch antenna of J shape,” *Electron. Lett*., vol. 42, no. 20, pp. 1134-1135, Sept. 2006.

[23] J. Holopainen, J. Villianen, R. Valkonen, J. Poutanen, O. Kivekäs, C. Icheln, and P. Vainikainen, “Mobile terminal antennas implemented using optimized direct feed,” in *IEEE Int. Workshop on Antenna Tech, iWAT 2009*, Santa Monica, CA, USA, March 2-4, 2009.

[24] K. S. Ang, Y. C. Leong, and C. H. Lee, “Analysis and design of miniaturized lumped-distributed impedance-transforming baluns,” *IEEE Trans. Microw. Theory Tech.*, vol. 51, no. 3, pp. 1009-1017, Mar. 2003.

[25] N. Marchand, “Transmission line conversion transformers,” *Electron. Lett*., vol. 17, pp. 142-145, Dec. 1944.

[26] M. C. Tsai, “A new compact wideband balun,” in *IEEE Microwave Millimeter-Wave Monolithic Circuits Symp. Dig.*, 1993, pp. 123–125.

[27] S. A. Maas and K. C. Chen, “A broad-band, planar, doubly balanced monolithic *Ka*-band diode mixer,” *IEEE Trans. Microw. Theory Tech.*, vol. 41, pp. 2330–2335, Dec. 1993.

[28] High Frequency Structure Simulator (HFSS). Ansoft Corporation, Pittsburgh, PA, 2001.